Phase Dependent Variation in the Reflectivity of Kuiper Belt Object 2002 MS_4

by Jinghan Peng

B.Sc., University of British Columbia, 2017
M.Sc., University of Victoria, 2023

A Thesis Submitted in Partial Fulfillment of the
Requirements for the Degree of

MASTER OF SCIENCE

in the Department of Physics and Astronomy

Phase Dependent Variation in the Reflectivity of Kuiper Belt Object 2002 MS_4

by Jinghan Peng

B.Sc., University of British Columbia, 2017
M.Sc., University of Victoria, 2023

Supervisory Committee

Dr. J J Kavelaars, Co-Supervisor

Department of Physics and Astronomy

Dr. Jon Willis, Co-Supervisor

Department of Physics and Astronomy

ABSTRACT

The Kuiper Belt Objects (KBOs) are the newly-discovered solar system objects located beyond the orbit of Neptune. Observations and study of the KBOs are vital to understanding the origin and evolution of our solar system. The KBO $2002MS_4$ is a large KBO, dwarf planet, and is my research focus. In order to study the physical properties, I used archival observations from the 3.6 m Canada-France Hawaii Telescope on Maunakea in Hawaii, combined with observations from the New Horizon spacecraft, to derive 2002 MS_4's rotational period and phase function. I find that this object does not have an obvious opposition surge and that the phase coefficient / geometric albedo correlation of 2002 MS4 is inconsistent with the correlation expected for C-type asteroids, casting doubt on the concept that C-type asteroids originated in the Kuiper belt. Using occultation observations, obtained at Anarchist Mountain Observatory, I determine an estimate of the minimum size of 2002 MS4 of $D > 820 \pm 20km$, consistent with other occultation measurements of $D = 800 \pm 20km$. This size is smaller than that derived from thermal observations where 2002 MS4 is modeled as a zero-spin body. The reasonable resolution of this result is that 2002 MS4 has a thermal inertia that must be included in its thermal model, which is left for future work.

Contents

List of Tables

List of Figures

ACKNOWLEDGEMENTS

I wish to recognize and acknowledge the very significant cultural role and reverence that the summit of Maunakea has always had within the indigenous Hawaiian community. I am most fortunate to have had the opportunity to obtain observations from this mountain.

This research used the Canadian Advanced Network For Astronomy Research (CANFAR) operated by the partnership of the Canadian Astronomy Data Centre and The Digital Research Alliance of Canada with support from the National Research Council of Canada the Canadian Space Agency, CANARIE, and the Canadian Foundation for Innovation.

I believe I know the only cure, which is to make one's centre of life inside of one's self, not selfishly or excludingly, but with a kind of unassailable serenity-to decorate one's inner house so richly that one is content there, glad to welcome any one who wants to come and stay, but happy all the same in the hours when one is inevitably alone.

Edith Wharton

Chapter 1

Introduction

The Kuiper Belt, a part of trans-Neptunian region, is a newly explored zone of the solar system. Trans-Neptunian objects (TNOs) are solar system objects with orbital semi-major axis beyond the orbit of Neptune, which is approximately 30 AU. The first Kuiper belt object (KBO) after Pluto was discovered in 1992 [44]. Observational techniques used to examine these objects are still in development but are largely based on examining solar light reflected as these objects are extremely faint at thermal wavelengths. In order to explore their properties (such as size, shape, albedo, multiplicity, etc.), a range of observational techniques are used. Indirect observations (e.g., reflected light planetary photometry, a stellar occultation by the KBO, orbital alignment as a signature of gravitational effects, and others) are the primary means of exploring the trans-Neptunian population. The opportunity to combine *in situ* spacecraft observations with Earth localized observing has only recently emerged. Two TNOs, Pluto and Arrokoth, have been visited by spacecraft (New Horizons), providing detailed observations of their surfaces (as well as that of Pluto's moon Charon) [74, 77]. These combined observations provide an unparalleled opportunity to understand a subset of the KBO populations fully. Studying KBOs provides a window into the early phases of planet formation. Their size distribution, especially in the kilometer-size range, represents a signature of the initial planetesimal formation process [67]. With the advent of the GAIA space-based astrometric reference frames and related high-precision astrometry, the use of occultations to explore the KBOs is rapidly advancing [e.g. 14, 17, 57]. Occultation observations provide a measure of the size of the body and enable the determination of the object's albedo. Measurements of albedos for individual objects can then be used as proxies for the albedos of KBOs from similar classes and relate the material of the Kuiper belt to other solar system populations.

Planetary scientists have gradually understood that a subset of the KBOs formed into so-called dwarf planets. This evolution in understanding has resulted in the former planet 9 of the solar system, Pluto, being reclassified as a dwarf planet. Detailed studies of the dwarf planet KBOs inform, in particular, the 'run-away' phase of planet formation [94]. At present, the dwarf population in the Kuiper Belt includes the well-known objects Pluto, Eris, Makemake, and Haumea.

Due to the great distance to the KBOs and their dark surfaces, studying these objects is technically challenging. Recently, the availability of large (diameter$>$ 3 m) optical telescopes (e.g., Canada-France-Hawaii Telescope, Gemini, Keck) and large space-based telescopes operating at thermal wavelengths (e.g., ALMA, Spitzer, and Herschel) are transforming our understanding of the dwarf planets of the Kuiper belt.

1.1 Classification of KBOs

1.1.1 Orbital properties

KBOs are divided into several dynamic classes. In the nomenclature defined by [30] we have:

- Scattering: Objects whose semi-major axis are changing by more than 0.1 au on timescales of less than 10 Myr, generally with pericentre near 35 au.
- Resonant: Objects whose orbits are in resonances with Neptune, the mostly populated resonance being the 3:2 mean motion resonance.
- Classical: Non-scattering, Non-Resonant objects. This category is often further sub-divided into *inner* (a$<$ 39.7 au), *main* (39.7 au $< a <$ 47.2 au) and *outer* with ($a >$ 47.2 au).

Among the main classical belt objects, there exists further dynamical sub-divisions, the major on being between those with low ($i < 5^o$) and high ($i > 5^o$) orbital inclination, often called the 'cold' and 'hot' components.

1.2 Surface colour properties

The colour of a KBO indicates its surface material. Specifically, an object will have a gray colour if its surface material absorbs nearly equal wavelengths of optical light. In contrast, an object will have a red colour if its surface is more prone to absorbing shorter rather than longer wavelengths of optical light. Complex organic molecules are known to absorb shorter wavelengths efficiently. Thus, optical colours of KBOs can be used to characterize the importance of complex organic molecules on their surfaces.

The colour of the surface of a Kuiper belt object is correlated with its orbital classifications and appears to be related to its formation conditions. These models predict a uni-modal distribution of KBO colours with some observation of colour variability during object rotation. However, it has been found that such a model does not explain the observed colour bi-modality [83, 84]. A survey by Tegler et al. [80] revealed two distinct colour groups and concluded that the colour bi-modality is most likely related to the primordial formation conditions [81].

With larger samples and multiple surface colour index values one can arrange KBOs in series of taxinomic classes, as has been done for the asteroid belt. Barucci [3, 4] define four taxonomic groups BB, BR, IR and RR for the population based on high-quality colour indices of B-V, V-R, V-I and V-J. Specifically, the group BB contains objects with neutral colour and RR those with very red colour, while the others have intermediate behavior. Work from Fraser [25, 26] has further explored the nature of the bi-modality and surface taxonomy finding only two distinct surface types with the intermediate classes being composed of a mixture of two end point compositions. Recently, Peixinho[59] have shown that different dynamical classes of KBOs and different sizes of KBOs have different colours. Both the four and two taxonomic class approaches, however, provide further evidence of distinct colour/dynamics relationships. The surface properties of KBOs appear to relate to their formation, rather than evolutionary, conditions.

The migration of outer planets is thought to have disrupted the primordial disk of icy planetesimals [50]. During such a disruption objects from different regions would have been scattered into dynamically hot orbits. On the other hand, dynamically cold KBOs were farther away from the migrating outer planets so that they were not scattered onto dynamically hot KBOs orbits. Objects in the hot and cold dynamical classes appear to also split between two colour classes, suggesting a link between this formation scenario and the observed colour distributions.

In this thesis, I will conduct a detailed examination of the dwarf planet 2002 MS$_4$. 2002 MS4 is the largest unnamed object in the Kuiper belt, specifically, it is in the top 15 largest object from roughly 4000 KBOs. Discovered in 2002 [87] this object is on stable (not scattering) ‘hot’ KBO orbit ($i \approx 17.7^o$) and in the main Kuiper belt ($a \approx 41.9$ au). The goal of this examination is to explore the current nature of 2002 MS4 and attempt to link this object’s orbital and physical properties to its possible formation location. This examination will include ‘mining’ archival data from different observatories, predicted occultations, and in-situ spacecraft observations. Specifically, this dissertation will investigate 2002 MS_4 (MS4 hereafter) in the following ways:

- Photometric properties (e.g., colour, low-phase angle scattering, and rotational light-curve) using archival Canada-France-Hawaii Telescope (CFHT) MegaCam observations.
- Size as determined from stellar occultations observed with a small (~ 30 cm) telescope at Anarchist Mountain Observatory.
- Surface texture by combining ground-based photometry and occultation-based sizes with *in situ* observations obtained with NASA’s New Horizons spacecraft.
- Discussion of thermal properties of MS_4 as determined from the above information and reported thermal flux measurements from the Spitzer and Herschel space observatories.

I will combine these observations into a portrait of the physical nature of this distant world.

The dissertation is organized as follows.

Chapter 2 provides detailed descriptions of the various observational and analysis methods and terminologies used in the thesis. In Section 2.1 optical telescopes and CCD detectors are introduced. In Section 2.4 I describe celestial coordinate systems and reference frames to which observations are calibrated and the data reduction processes. The fundamentals of photometric observations will be explained in Section 2.6. In this section I introduce important concepts for this thesis, such as magnitudes, filters, and photometric systems. Photometry for planetary bodies has a different origin and nomenclature compared to stellar photometry and some terms specific to planetary photometry will be introduced. In particular, the various types of albedos, such as geometric albedo, Bond albedo, single-scattering albedo, etc, are explained. I describe my analysis techniques for measuring and calibrating the reflected light flux from the MS4. In Section 2.8.1 I describe light curves (time variable flux measurements) and how the body's rotation period can be obtained; three often used methods will be introduced. And in Section 2.8.2 various models to describe and derive the phase curve (viewing geometry variations in measured flux) are detailed. Section 2.9 provides some background on stellar occultation by a KBO. Key factors for occultation reduction are explained together with detailed formulae. Finally, I derive a statistical approach for estimating an occulter's diameter based on independent single-chord observations.

Chapters 3 and 4 provide the main results of this thesis. In Chapter 3, the photometry of MS4 is described in detail. Detailed procedures and high-precision measurements of the rotation period and phase curve of 2002 MS4 are given. I derive a rotational period for MS4 (T=14.251 h), furthermore, obtain MS4's low solar phase function after correction for rotational light-curve effects. Combining these data with observations of MS4 from the New Horizons spacecraft, a complete phase function of MS4 is delivered.

In Chapter 4, I present detailed information on two single chord observations of the occultation by 2002 MS4. The probable radius of MS4 is derived and compared to existing literature values. The geometric albedo and phase integral are determined.

In Chapter 5, I summarize my results on the measurement of 2002 MS4 determined from the observations presented. I conclude with suggestions for future work.

Chapter 2

Observational Methods

2.1 Telescopes

A telescope enables one to observe dim objects, often at large distances. The first person to apply for a patent for a telescope was Dutch eyeglass maker Hans Lippershey (or Lipperhey) ([46]). In 1608, Lippershey claimed a device that could magnify objects thrice. His telescope had a concave eyepiece aligned with a convex objective lens. One story goes that he got the idea for his design after observing two children in his shop holding up two lenses that made a distant weather vane appear close. Others claim he stole the design from another eyeglass maker, Zacharias Jansen. Afterward, other scientists, including Galileo Galilei and Isaac Newton, made changes to the initial model for better accessibility and quality of images. Early telescope design was concerned with using combinations of lenses to provide a magnified view of distant objects.

The two primary types of telescope are reflecting and refracting telescopes. Refracting telescopes use only lenses in the optical system, while reflectors use a curved mirror to redirect light to a focal point and may use lenses or additional mirrors to focus the light coming from the main/primary mirror onto an imager or spectrograph. Refracting telescopes are limited in their size due to the complexity of manufacturing physically large lenses. Reflecting mirrors as large as 8.4 m diameter have been manufactured and used in astronomical telescopes [41]. Even larger reflecting telescopes have been built from a mosaic of individual mirrors tuned to focus the light on a common element. The use of large primary optics enables gathering a large area of light and then focussing that light onto a single image. The availability of ever-larger telescopes enables the exploration of ever-fainter astronomical sources.

Two properties characterize a telescope: the diameter of the objective lens or primary mirror (D) and the effective focal length (efl). The larger D, the more light-gathering power. The large efl, the larger the magnification. The $f/\#$, or focal ratio, is the ratio of the focal length (efl) and the diameter, D, of the primary mirror or objective lens

$$f/\# = \frac{efl}{D}.$$

With the same size primary, the larger the focal ratio, the longer distance from the primary to the focus. The larger the focal length, the more magnified an image will be at the focus. With the same focal ratio, the larger the mirror, the more concentrated the light.

The Field Of View (FOV) of the instrument corresponds to the angular extent of the sky that the instrument can 'see' and is determined by the size of the camera (w) and efl. An illustrative diagram of FOV is shown in figure 2.1. From the geometry, it is easy to find that

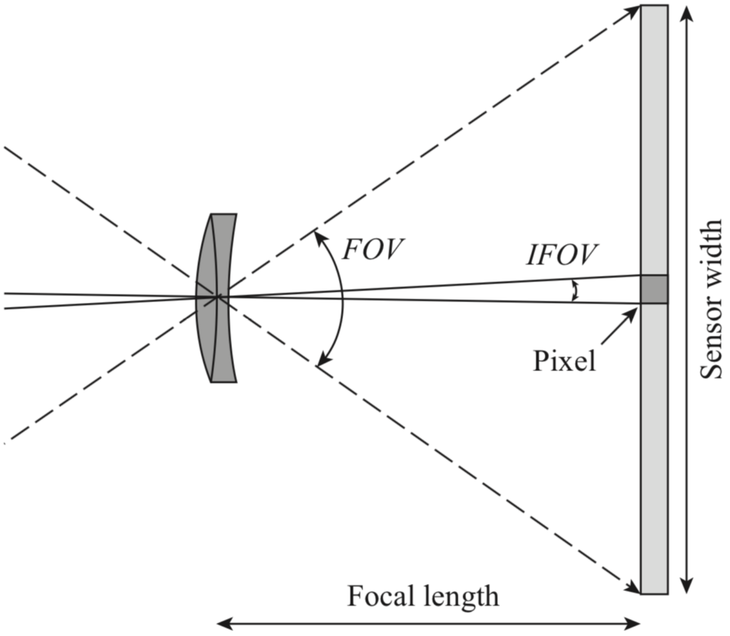

Figure 2.1: Field of view. From [68]

$$FOV = 2\tan^{-1}(\frac{w/2}{efl}),$$

where w is the sensor width. In the case when $efl \gg w$,

$$FOV \approx \frac{w}{efl}.$$

A telescope's plate or pixel scale is the image plane field of view per unit length. The scale is often given in arcseconds per pixel or radians per mm. For a single pixel in the FOV expressed above, one finds that the plate scale is given by

$$\text{plate scale} = \frac{206265}{D \times f/\#} \quad \text{arcseconds/mm}$$

when D is expressed in mm. The pixel scale determines the sampling of the image at the detector. The pixel scale should match the angular size of interest. Full-width at half maximum (FWHM) of the point spread function (PSF) of an image (also called seeing) is often used to express the resolution of a telescope. The PSF is the image shape made by a point source of light after passing through any atmospheric turbulence (for Earth-based telescopes) and the telescope's optical system. Adaptive optics counteract the atmospheric turbulence [63, 68] and provide the opportunity for higher resolutions. The FWHM has a theoretical smallest size θ determined by D and the wave nature of light. The limiting angular resolution θ of a telescope is approximately

$$\theta = 1.22\frac{\lambda}{D},$$

when $D \gg \lambda$, and λ is the wavelength of observation. A pixel-based imager can resolve angular scales that fall across two or more pixels (Nyquist sampling theory). The optimally designed imager for a given telescope will thus have 2 pixels per FWHM of the PSF.

For a telescope with $D = 4.0$ m the theoretical limit of resolution is $\theta = 1.22\frac{\lambda}{D} \sim 0.03''$ for $\lambda = 500$ nm (optical light). However, on Earth, the natural resolution is at best ~ 0.4 arcseconds due to turbulent motion in the atmosphere distorting the path of the light. For the case of optical imaging, natural seeing requires a pixel scale of ~ 0.2 arcseconds/pixel. Modern CCD detectors have a pitch of around 10 um per pixel, and thus the plate scale at the detector should be 0.2 arcseconds/10 um (0.0969 rad/m), which for a $D = 4$ m meter implies a desired focal ratio of

$$f/\# = \frac{1}{0.0969 \ \ \text{radians/m} \times 4m} \sim 2.5$$

.

For example, the Canada France Hawaii Telescope has a mirror with a usable diameter of 3.58 m and its wide-field-corrector imaging focus focal ratio of $f/\# = 4.18$ providing a plate scale of 0.1373 arcseconds per 10 um pixel.

2.2 The Charge-Coupled Device (CCD)

The charge-coupled device (CCD) has been widely used in astronomy since the 1980s. CCDs often have quantum efficiency (QE, fraction of photons impinging on the detector that are detected) of 80%-95% at optical wavelengths, while a photographic plate has a "QE" of much less than 10%. The nearly ten times higher QE of CCDs provides an enormous advantage. A second important benefit of CCD detectors is the very good linearity (a linear conversion between photons impinging on the detector and the electronic signal produced). The linearity of CCDs allows one to make high-precision comparisons between the intensities of different stars. Thirdly, a CCD camera is very convenient for obtaining a digital astronomical image without any operations such as developing, fixing, and digitizing a photographic plate. And storage in digital form makes it possible to engage in reproducible computation-based analysis rather than visual image inspection. Due to these various advantages, CCDs have now replaced traditional photographic plates.

One disadvantage, however, is the small physical scale of the CCD chip. For example, 1K × 1K, or 2K × 2K size chips, which are easily found in the market, cover only ~ 10 mm of the focal plane, while rectangular photographic plates of ~ 300 mm size were regularly in use. Larger CCDs, 4K × 4K, are rather difficult and costly to manufacture. Much greater sizes, such as 10K × 10K, have been produced but are rare. A large field of view with critical sampling in astronomy is achieved by combining some smaller size CCD chips into a CCD mosaic.

An example of a CCD mosaic is the camera used by the Gaia space observatory of the European Space Agency. The Gaia camera has a 106 CCD mosaic focal plane (Figure 2.2). The Gaia observatory provides high-precision astrometric observations of bright stars, which are used to compute a precise astrometric reference frame to calibrate other images. These precise calibrations enable more accurate determinations of positions of objects like TNOs and have been critically important to enable predicted occultations of stars by these objects.

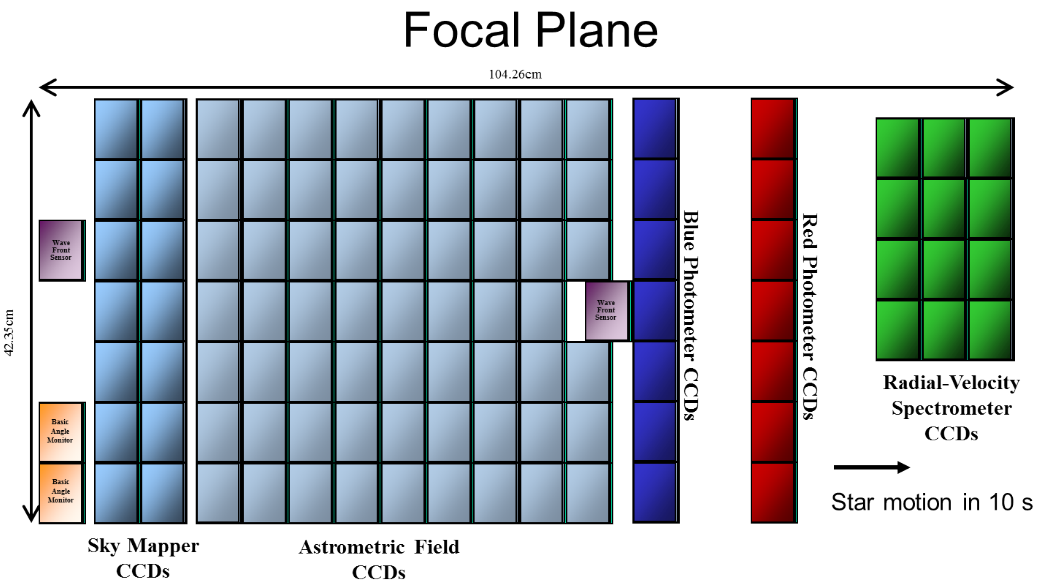

Figure 2.2: Gaia focal plane. From https://gea.esac.esa.int/

2.3 Telescopes and detectors used in this work

In this thesis, I present the analysis of imaging data taken by three different telescope/camera systems. In Section 3.1 I present photometric observations of MS4 obtained using the MegaCam CCD mosaic imager [12, 20] mounted at the F/4 prime-focus of the Canada-France-Hawaii Telescope (CFHT, see Figure 2.3). The CFHT is a 3.6 m telescope located on Maunakea, a 13,800 feet elevation dormant volcanic mountain on the “Big Island” of Hawaii. In Section 3.3 I present observations obtained using the Long Range Reconnaissance Imager (LORRI, [19]) on NASA’s New Horizon spacecraft. New Horizons explored the Pluto/Charon system [74] as well as the small Kuiper belt object Arrokoth [77]. LORRI is an f/12.6 Ritchey-Chretien telescope and camera system with an aperture of 20.8 cm diameter and a FOV of about 0.29 degrees. LORRI’s CCD imager is 1024 × 1024 pixels [19]. LORRI has no filters, and the CCD is photon sensitive from 350 nm to 850 nm with a central wavelength of about 600 nm. The LORRI pixel scale is about 1 arcsecond per pixel. LORRI is being used to obtain white-light measurements of the photometric properties of some distant KBOs, including the TNO 2002 MS4.

Figure 2.3: MegaCam/CFHT. Download from https://www.cfht.hawaii.edu/

In Chapter 4 I present the measurements of occultations (see 2.9) of two separate stars by 2002 MS4. The observations were obtained using a 300mm aperture telescope with a f/4.9 imager focused onto a QHY-174M-GPS camera. The CCD has 5.86 um pixels providing a pixels scale of 0.8”/pixel. The telescope is located at the Anarchist Mountain Observatory (119.36W, 49.00N, 1086m) near Osoyoos, British Columbia, Canada.

2.4 Coordinate Systems and Frames

A coordinate reference system is a set of rules that defines the origin and orientation of a set of coordinate axes. A coordinate reference frame generally includes a set of distant objects whose coordinates, expressed in a particular system, provides a physical realization of that reference system. The International Celestial Reference System (ICRS) defines that all reference frames are to be ‘space coordinate grids with origins at the solar system barycentre or at the centre of mass of the Earth and show no global rotation with respect to a set of distant extra-galactic objects’ [7]. The International Celestial Reference Frame (ICRF) contains more than 200 primary and 3000 secondary sources whose coordinates have been well determined (some using Very Long Baseline Array observations). This work will express all coordinates in ICRF Equatorial Coordinates.

Similar to the Earth's latitude, we use declination (DEC δ) to count the position of an object relative to the north and south poles of the ICRS. DEC is zero at the equator and rises uniformly to $+90^o$ at the north pole and decreases uniformly to -90^o at the south pole. Right ascension (RA α) is used to measure the eastward angular position, similar to but reversed from longitude on Earth. The starting point i.e., zero degrees for RA is, colloquially, the vernal equinox, where the Sun crosses the celestial equator and moves to the north but in ICRS the axis is defined relative to the position of QUASAR 3C 273B as reported in [39]. Similarly the pole of the ICRS is fixed using the observations of QUASARS and remains fixed to +/- 20mas. Prior to the adoption of ICRS, astronomers provided coordinates relative to the location of the Sun at the vernal equinox, a position that changes due to the precession of the Earth's spin axis and other periodic variations in the Earth's orientation relative to the Sun. Due to this motion such coordinates are expressed with an epoch, examples include B1950 and J2000 which are relative to the pole on 1 January 1950 and 1 January 2000. ICRS was defined to match the J2000 coordinates, but, in fact, is slightly (a few 10s of mas) misaligned [24]

Equatorial and Ecliptic coordinate frames (see figure 2.4) are commonly used in planetary science. The origins of both systems can be either the Sun or the Earth and they are called heliocentric or geocentric coordinate systems. The equatorial system is commonly used for telescopic observations while the ecliptic system is more convenient when considering descriptions of the structure of the solar system. Observations of a source within the solar system can only be fully characterized when the distance to the source is also specified. Once the distance and ecliptic coordinates are known, the full geometry of the observation (see Figure 2.5), in particular the phase angle of the observation, can be determined.

Knowing a set of object coordinates in a particular reference frame enables us to determine the a relation between the image pixels values and the coordinate frame values. These relationships are known as the World Coordinate System (WCS) transforms. With the WCS transform one can determine the coordinates of other objects within those images. This work uses the Gaia DR2 catalog [15] as set of secondary ICRF reference coordinates. Gaia DR2 positions, derived from the primary IRCF values, are precise to better than 10 μ'' and provide a high enough sky density of sources that they can be used to calibrate individual CCD frames. Note, when using secondary stellar reference stars from Gaia I also account for the star's proper motion but these motions are quite minor compared to the centroiding precision of our target sources.

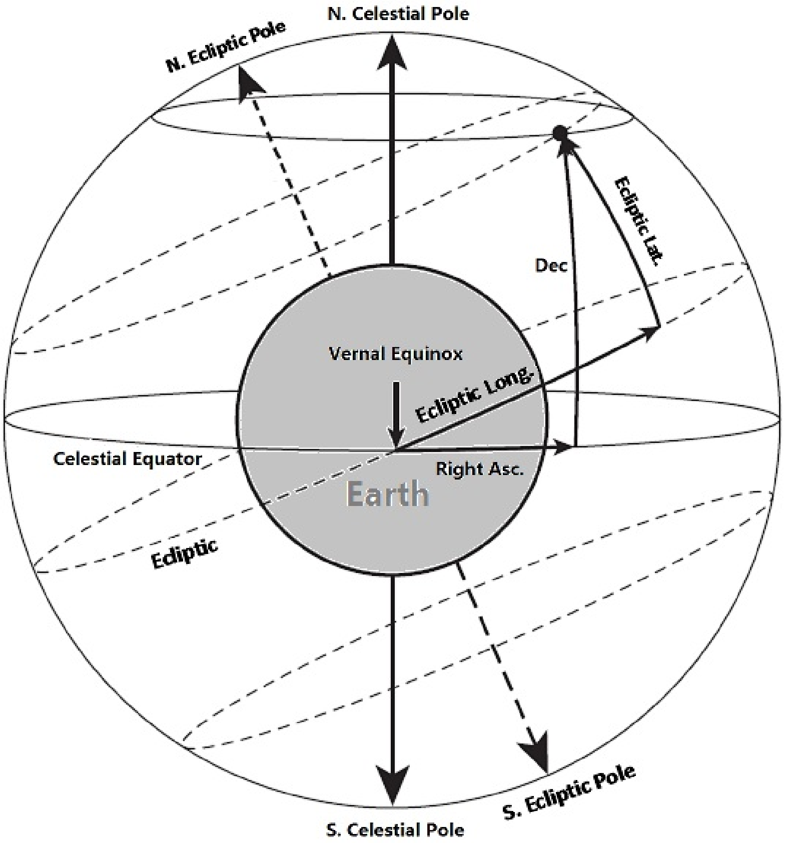

Figure 2.4: The equatorial and ecliptic coordinate systems with the Earth as the origin. Coordinates can be represented in either the right ascension and declination (RA/DEC) or ecliptic longitude/latitude.

2.5 Observing Circumstances

For a solar system object, it is convenient to express its position with respect to the Earth and Sun. Figure (2.5) shows the relationship between a solar system body and the Earth-Sun system in a relative coordinate perspective. The related concepts are listed as follows,

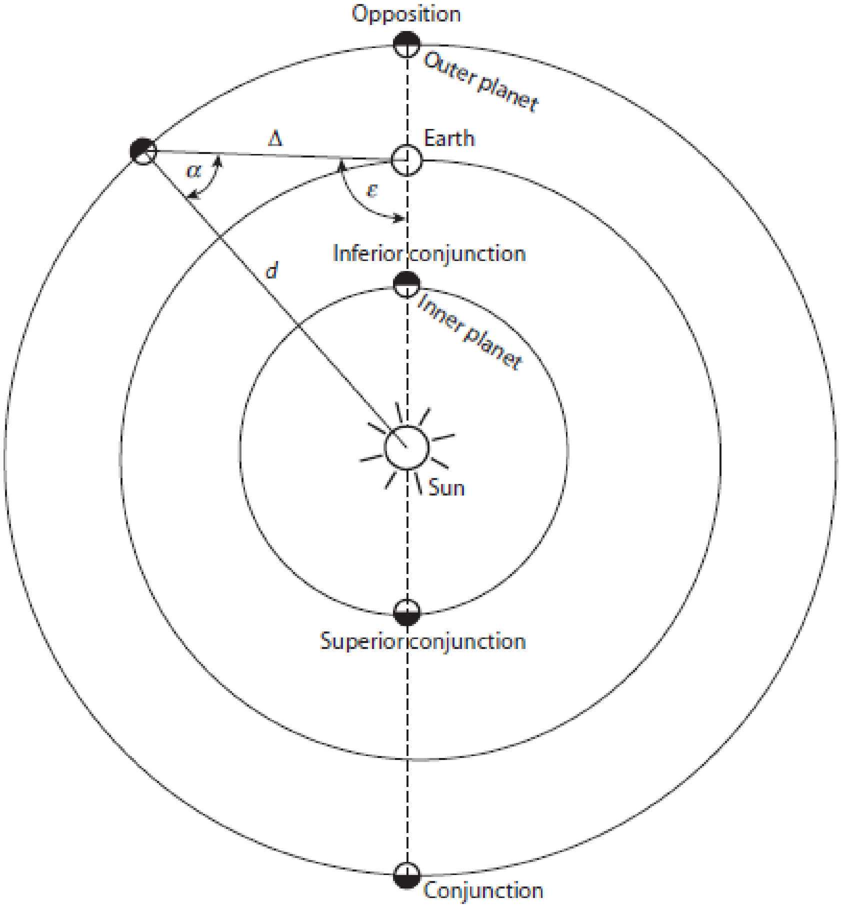

Figure 2.5: Relative coordinates for a solar system object. Credit: Michael K. Shepard [68]

- Opposition: When an outer planet is directly opposite the Sun from the Earth, it is located at the opposition point. Opposition is the convenient time to make observations of a source as the visible surface is fully illuminated.

- Conjunction: When an outer planet moves to the opposite side of the Sun from the Earth, it is at conjunction. On the other hand, for interior planets, when it is aligned with the Earth and Sun, it is also at conjunction. More exactly, it is referred to be at inferior conjunction when the planet is between the Earth and Sun and at the superior conjunction when on the opposite side of the Sun (see Figure 2.5)

- Elongation: The angle between the line from the Earth to the Sun and the line from the Earth to a planet is called solar elongation.

- Phase angle: The angle between the line from a planet to the Earth and the line from the planet to the Sun is called the phase angle. It is straightforward to see that the location of zero phase angle for an outer planet will happen at two locations. One is when the planet goes through opposition, and the other is when the planet goes through conjunction. When an outer planet goes through opposition, a 0-degree phase angle requires the planet to be 180 degrees away from the Sun in right ascension and fall on the ecliptic plane.

In this thesis I will present analysis of observations of 2002 MS4 taken near opposition, to determine its light curve variation, and data taken off opposition to determine the phase variation in that light curve.

2.6 Magnitudes and Photometric Systems

The irradiance, E, is the radiated power over all wavelengths, incident on a unit area of a receiver. It's often used to measure the luminous intensity of the Sun. A related term, spectral irradiance F, is defined if we want to describe the flux for a particular special wavelength range:

$$F = \frac{dE}{d\lambda}.$$

The radiant intensity, I, is often used to measure the light power for an unresolved source. It is the power measured in a unit solid angle of the receiver.

$$I = \frac{dp}{d\Omega}.$$

In this section I will describe the set terms commonly used in planetary science to describe the various measurements of the observed and absolute irradiance of planetary bodies, the wavelength ranges over which those irradiance values are measured and the reference systems used to express those measurements .

2.6.1 Magnitude

Magnitude is used to quantify the brightness of an object by comparing the irradiance of one celestial body to that of a standard celestial body (or system). In modern usage, the magnitude of source is negative 2.5 times log (based 10) of the flux plus some arbitrary scale offset. Historically, people compare the received irradiance from Vega (α Lyra) to the irradiance from the object of interest:

$$m_{Vega} - m_{object} = -2.5log(\frac{E_{Vega}}{E_{object}}) \tag{2.1}$$

Nominally the magnitude of a source is reported for a specific wavelength range. The range of wavelength of a particular measurement is determined by the use of an interference filter. To correctly report the flux of source across a specific wavelength range in a coherent way requires the adoption of a set of reference fluxes. In this thesis I report the measured magnitude of 2002 MS4 in the CFHT MegaCam system and then transform it to that in the SDSS filter system calibrated to the AB (absolute) magnitude system.

Instrumental Magnitude

Instrumental magnitude is the 'raw' magnitude measured directly from CCD image.

$$m_{ins} = -2.5log_{10}(n_e) = -2.5log_{10}(ADU \times gain),$$

where ADU is the number of analog units recorded by the detector electronics and the $gain$ is the ratio factor to transform the number of ADU to the number of electrons n_e that were recorded.

Apparent Magnitude

The apparent magnitude of a celestial body is its magnitude as seen by the observer, the instrumental magnitude, expressed in some standard magnitude system. A standard magnitude system is an agreed on calibration between the magnitude values and some reference source or sources. An object's magnitude given in a standard magnitude can be directly compared to a magnitude in a catalog, e.g., an object magnitude in Johnson V or SDSS r. One obtains the apparent standard magnitude by comparing the irradiance of a target with that of a standard source (i.e. a star with an irradiance that is known *apriori*) observed with the same facility and at the same angle through the atmosphere under similar conditions, i.e.,

$$m_{app} = m_{standard} - 2.5log_{10}(\frac{E_{target}}{E_{standard}})$$

The apparent magnitude of a body is not constant but depends on the intrinsic properties of the object at the time observation and the observing geometry. Variations in reflectivity, shape, orientation, rotation axis, viewing angle, and distance from the observer or illuminator can all change the apparent magnitude of a planetary body. In planetary science the apparent magnitude is normally referenced as $m_{app}(d, \Delta, \alpha)$ with d the distance to the Sun, Δ the distance to the observer, and α the phase angle of the observation.

Reduced Magnitude

The reduced magnitude, $m(1, 1, \alpha)$, also called unity distance magnitude, removes the effect of both observer and illuminator distances while leaving the effect of phase of the observation. The reduced magnitude can be determined as

$$m(1, \alpha) = m_{app} - 5log_{10}(d) - 5log_{10}\Delta. \tag{2.2}$$

Reduced visual magnitude represents the reduced magnitude in the standard V band, denoted by $V(1, \alpha)$. $V(1, \alpha)$ measures are used to determine the phase curve, which is the planetary body's reduced visual magnitude variation with phase.

Absolute Magnitude

Absolute magnitude is conceptual, representing the apparent magnitude at Δ=1 AU, d= 1 AU, and $\alpha = 0^o$. In reality, no observer can satisfy this geometry. The absolute magnitude is estimated using a measure of the phase curve and observations of the source at known distances. The absolute magnitude is normally given in the visual band, unless an alternate band is specified, and written as $V(0)$ or H and $H(0)$. For asteroids that rotate, the mean brightness of the light curve is used when computing the absolute magnitude [68]. We shall note that in stellar astronomy the absolute magnitude is the magnitude of a given source if that source were viewed at a distance of 10 parsec.

2.6.2 Photometric Systems

A photometric system is a combination of telescope, sensor and filter used, these are commonly referred to as a telescopic systems. A standard photometric AB magnitude system is well calibrated telescopic system where the zero point has been calibrated to an absolute flux references.

Interference filters restrict the range of photon wavelengths that are able to enter the detector. The UBV filter system, developed since the early 1950's [10] and the Sloan Digital Sky Survey (SSDS) $ugriz$ filter set [27] are the two multi-filter magnitude system used most widely in astronomy. In any multi-filter system, a color index is defined as the difference of magnitudes measured through two different filters. For example, by subtracting the B magnitude from U in UBV system, we get the color index $U - B$. The work in this thesis makes use of measurements obtained using filters designed to match the SDSS $ugriz$ system.

Johnson-Cousin $UBVRI$ System

The star Vega (α Lyra) defines the zero magnitude (zero point) of the $UBVRI$ system [68] By definition, V_{Vega} is zero and the colour indices are also zero. Subsequent to the definition of the $UBRVI$ filter band passes, observations by Hayes and Latham [38] shifted the zero point to be a flux of 3500 Jy at wavelength 555.6 nm so that V_{Vega}=0.03 while its colour index values remain zero. In practise, people frequently use the Landolt stars [49] as a list of reference stars to compare to the target instrumental magnitude and thus obtain the target magnitude in $UBVRI$ system. Observations with a particular telescope/instrument combination are calibrated to the Landolt standards via series of photometric transforms that connect that telescope's instrument system to the $UBVRI$ system.

Oke AB System

The AB system is divorced from the practise of using a particular star as zero point and AB stands for absolute. Oke defined the AB system zero point to be a flux density $f_{\nu o} = 3.63 \times 10^{-20}$ergs $s^{-1}cm^{-2}Hz^{-1}$ in all band passe [54]. This number is decided such that M_{AB} around 548 nm corresponds nearly to visual magnitude V for all stars. Therefore, the AB magnitude of a target will be

$$M_{AB} = -2.5log_{10}f_{\nu} - 48.60,$$

where f_{ν} is the flux density of any particular band pass.

The Oke AB system consists of a series of narrow bandpass filters, each only 4 nm wide. There are 68 bands between wavelengths of 308 nm and 1200 nm [10]. Oke's zero point is derived from spectral observations of 38 white dwarf stars compared with theoretical models to derive absolute fluxes and temperatures. Using filters tied to the AB system enables the determination of the absolute irradiance from a source, rather than the irradiance relative to some arbitrary reference point.

Sloan Digital Sky Survey *ugriz* System

The Sloan Digital Sky Survey (SDSS) system consists of five broad band filters ($u'g'r'i'z'$) that cover the wavelength range of 300 nm (atmospheric UV cutoff) to 1100 nm (silicon sensitivity limit). Table 2.1 includes the details on filter central wavelength λ_c and the band width $\Delta\lambda$ in nm.

Table 2.1: The centering wavelengths and pass bands in nm for SDSS [27].

filter	center λ_c(nm)	$\Delta\lambda$(nm)
u'	350	60
g'	480	140
r'	625	140
i'	770	150
z'	910	120

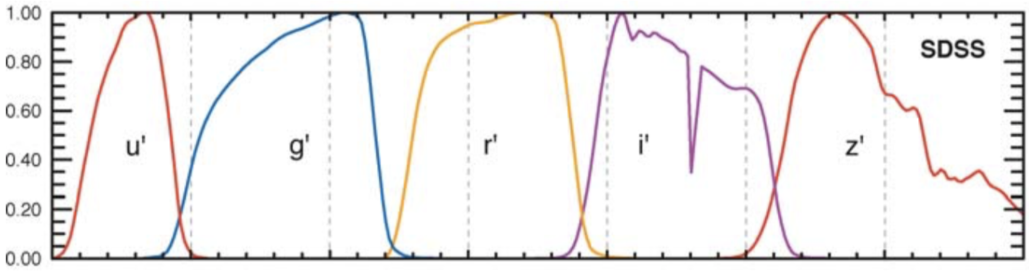

Figure 2.6: The response curves for the SDSS filters.

SDSS aims to tie the natural photometric system to the absolute flux by using the AB system zero point[29]. A hypothetical object with flat spectral distribution with flux density $f_{\nu o}$ has AB magnitude $M_{AB} = 0$ over all frequency bands [28]. This AB mag zero point system can be extended to any filter system, given that the photon counts representing the zero point flux ($f_{\nu o} = 3.63 \times 10^{-20}$ergs $s^{-1}cm^{-2}Hz^{-1}$) are measured through the new set of filters [28]. Four metal-poor subdwarf stars BD+17°4708, BD+26°2606, HD 19445 and HD 84937 are used as zero point reference stars as described in the AB system by Oke and Gunn [55]. It is worth noting that even though inteneded to define the zero-point with absolute flux, the SDSS actual photometric zero-point has been found to have small offset from the AB system. The u' band zero point is in error by 0.04 mag, z' band by 0.02 mag and other bands $g'r'i'$ by around one percent, approximately 0.01 mag. Figure 2.6 shows the response curves for the SDSS filters. Irradiance values reported as SDSS AB magnitudes are given the designations $ugriz$ (i.e. the prime of the SDSS filter system is removed).

Observation obtained at various telescopes (whose optics, detector and filter system will, necessarily, differ somewhat from the SDSS or Johnson systems) must first be tied to a standard photometric system before they can be used in a comparative analysis. This procedure is conventionally called photometric calibration and can be achieved by a variant of the Fundamental Reduction Formula:

$$M = [m - k'_f X - k''_f XCI] + T_f(CI) + ZP_f \tag{2.3}$$

[92]. Where, M is the resulting standard magnitude of the target, m is its instrumental magnitude, k_f is the first order airmass[1] coefficient, k_f is the second order airmass coefficient, X is the airmass, CI is the colour index of the object, T_f is the transformation for filter f from observational instrument to the standard magnitude instrument, and ZP_f is the nightly zero point for filter f.

2.7 Albedos

A distant solar system object, either a disk-resolved object or a disk-integrated one, is detected via the solar light it reflects. The fraction of light reflected from the surface is defined as the geometric albedo of the source.

In quantifying the light scattering properties of a planetary surface or laboratory sample a number of different albedos are defined. For some albedo values a perfect Lambertian is the reference while for others the total incident energy is the refernce. Sometimes, in order to explain the intrinsic reflectivity for a specific area of a target planet, the detailed radiance for an area at specific illumination and reflection angles at a variety of wavelengths are needed, this is the wavelength dependent phase curve of the surface material. The various albedos are defined to enable convenient and accurate discussion a target object and I give here definitions of the

---

[1] the fractional amount of atmosphere one is looking through where 1 indicates the mean amount of atmosphere at sea level

albedo concepts used in this thesis.

Geometric Albedo

The geometric albedo, also named physical albedo, p, is the ratio of the radiant intensity (over all wavelengths), $I(0)$, of a planetary body to the radiant intensity of a Lambertian disk, I_{Lam} of the same cross-sectional size. Both the planetary body and the Lambertian disk are in the opposition configuration relative to the Sun and located at the same distance from the Sun. The geometric albedo is defined as

$$p = \frac{I(0)}{I_{Lam}}$$

This parameter indicates the 'rate of reflectivity' of the target compared with a standard Lambertian model. An important point to notice is that the radiant intensity ratio is between the planetary surface and a Lambertian DISK of the same cross-sectional area, NOT a Lambertian sphere. Lambertian is used as comparison as it assumes that an object reflects light uniformly in all directions, regardless of the incident angle of the light. This simplification makes calculations and analysis more tractable. In practice, the geometric albedo usually refers to a specific wavelength range (e.g., the visual albedo at 500-600 nm) instead of over all wavelengths. The geometric albedo is then determined as,

$$p_V = 10^{0.4(m_{sun}-H)}(\frac{\pi r_{au}^2}{a}), \tag{2.4}$$

where m_{sun} is the apparent magnitude of the Sun and H is the absolute magnitude of the planetary body, r_{au} is the distance of one astronomical unit and a is the projected area ($\frac{\pi D^2}{4}$) of the planetary body [42]. If the geometric albedo is known then Equation 2.4 and be rearranged to provide the size of the object (taking $m_{Sun} = -26.76$ [9]),

$$D = 10^{0.2(m_{sun}-H)} r_{au}(\frac{4}{p_v})^{\frac{1}{2}} = \frac{1330}{\sqrt{p_V}} 10^{-0.2H_V} \tag{2.5}$$

Geometric albedo is particularly useful for comparing the reflectivity of different objects and for understanding the intrinsic properties of an asteroid's surface. It provides information about the object's overall brightness at a particular phase angle.

Bond Albedo The Bond albedo is the ratio of reflected light over the total amount of light incident on the planetary surface. The total amount of incident light has only the scattered (or reflected) component and the absorbed components assuming the planet have no source or producing no energy inside.

If the geometric albedo is known, we can derive Bond albedo (A) by

$$A = pq, \tag{2.6}$$

where q is the phase integral. The phase integral is the weighted average of scattering over all phase angle defined by

$$q = \int_0^\pi \Phi(\alpha) \sin(\alpha) d\alpha,$$

where, $\Phi(\alpha)$ is the integral phase function, which varies depending on the type of surface model we decide to apply. In other words, it quantifies how the reflectivity of the object changes as it is observed from different angles relative to the Sun. Often the visual band geometric albedo is used in Equation 2.6 as the substantive majority of the solar flux is in the optical bands. Bond albedo is useful for understanding the energy balance of an object in the solar system. It takes into account how much energy the object absorbs and re-emits, which is important for studying the object's temperature and climate. It is especially valuable for comparing the energy budgets of different celestial bodies.

Single-Scattering Albedo The single-scattering albedo (also called volumetric single-scattering albedo [33]) (w or ω) in the general photometric scattering model has a similar meaning as the Bond albedo but on a micro-scale. Assuming the incident photon can only be reflected once or absorbed, w is defined as the ratio of scattering cross-section and the sum of scattered and absorbed cross-sections. A surface made from transparent material scatters more, and its w approaches 1, whereas highly absorbing material has w approaching 0.

Visible Albedo Radiance factor r_f also called apparent albedo or visible albedo is the ratio of the radiance of a sample at some incident, emission and viewing angle to the radiance of a Lambertian sample viewing from overhead.

$$r_f = \frac{L(i, e, \alpha)}{L_{Lam}(0, 0, 0)}$$

Apparent albedo can be bigger than 1 at some illumination and viewing configurations, but summed over all areas on the planetary surface the total energy is conserved.

2.8 Disk integrated photometry

For a disk-integrated photometry of airless bodies, such as asteroids and KBOs, we required accurate measurement of the magnitude and its variations with respect to time and phase angle. The goal of these measurements is to characterize the physical properties of the object including rotation period and surface composition by measuring the light reflected off the surface at different phases of the objects rotation and at different phase angles of observation.

Here I discuss three methods to solve for a rotational light curve. Using this information I then show how the absolute magnitude of the source can be determined. The absolute magnitude of the source as a function of phase angle of observations can then be used to fit various standard phase function models. I describe some phase effects and models designed to parameterize these effects.

For photometric observations (usually reported as reduced magnitudes) of a solar system object, the phase curve and light curves naturally entangle to form its apparent magnitude, changing with time and solar phase angle also. However, these two source of brightness variation occurs on different time scales. Phase curve variations occur over weeks and months as the phase angle change is related to the relative geometry between the Earth, Sun and target object. Rotational lightcurve variations occur on shorter time scales, normally over a few hours for solar system bodies [68]. Therefore, we first determine the period (for periods) of light curves taken over several days successive observations using the techniques in the next section. After removing the periodical changes from light curves, a phase dependent measurement of $\overline{H}(\alpha)$ can be derived.

2.8.1 Lightcurves

A rotation lightcurve captures the brightness change of an asteroid with time due to its irregular shape or varying albedo or both. As long as the asteroids is large enough, it can be assumed to reach its hydrostatic equilibrium. Then the variation due to its shape will be minimized. Generally, for small bodies, the albedo is treated as uniform over the body, which is consistent with the majority of spectroscopic and colour-photometric observations. For a period light curve of an asteroid, its brightness f at time t can be expressed using a Fourer series as follows,

$$f(t) = a_0 + \sum_{n=1}^{\infty} \left[a_n \cos(\frac{2\pi nt}{T}) + b_n \sin(\frac{2\pi nt}{T}) \right], \tag{2.7}$$

where, T is the rotation period, a_n and b_n are amplitude coefficients corresponding to the *sine* and *cosine* functions The constant a_0 gives us the mean brightness. The number of terms, n, is the harmonic order of the series.

Although Fourier series expansion is a well-known method to derive a period of a sampling sequence, unequal sampling is often encountered. A few techniques have been developed for the period determination from an unequal sampling sequence. Here, three approaches are introduced. Phase dispersion minimization [73] and 'Lomb-Scargle' least-squares frequency analysis [52, 66]. The 'Lomb-Scargle' method allows unevenly sampled input data by breaking the time series into a linear combination of *sin* and *cos* functions [58]. Harris [35] combines multiple lightcurve segments to perform Fourier analysis and uses a linear least square fit to determine the period taking photometric uncertainty into account.

Phase Dispersion Minimization (PDM)

Following Stellingwerf [73], suppose that we have a set of discrete observations (x_i, t_i), $(i = 1, N)$, where x_i is the observed magnitude, and t_i is the corresponding time. Let σ^2 be the variance of all x_i,

$$\sigma^2 = \frac{\sum_{i=1}^{N} (x_i - \overline{x})}{N-1}, \tag{2.8}$$

where, $\overline{x}$ is the mean of all observations,

$$\overline{x} = \frac{\sum_{i=1}^{N} x_i}{N}.$$

Now, divide the observations into a few (M) subsets. In each subset, the sample variance s_j^2 $(j = 1, M)$ is computed (as in Equation 2.8). For each s_j^2, n_j data points are included. Then the overall variance for all M samples becomes,

$$s^2 = \frac{\sum_{j=1}^{M}(n_j - 1)s_j^2}{\sum_{j=1}^{M} n_j - M}. \tag{2.9}$$

In order to minimize the variance of the data against the mean light curve, let T be a trial period, and compute a phase series like

$$\phi_i = \frac{t_i}{T} - [\frac{t_i}{T}].$$

Here, brackets mean the integer part. The data are grouped such that all members of j have similar ϕ_i, i.e. the phase interval (0,1) is usually divided into M subsets, nominally bins of fixed ϕ_i width. If a suitable or correct period is found, the variance of s_j^2 of the measures in a bin will be smaller than the global variance. If T is not a suitable value then the members of each of the M bins will be from different phases of the true light curve and $s^2 \approx \sigma^2$. The overall variance can be considered as a function of ϕ and the statistic,

$$\Theta = \frac{s^2}{\sigma^2} \tag{2.10}$$

, is used to determine the correct period. If T is the correct period then Θ will approach a minimum. As this technique minimizes the dispersion of the data in each phase bin the approach is termed ”phase dispersion minimization” (PDM).

Lomb-Scargle

Another technique to find a period for an unequally sampled data is the Lomb-Scargle algorithm. First proposed by Lomb [53] in 1976 and refined by Scargle [66] in 1982.

Suppose we have a discrete set of observations (x_i, t_i), $(i = 1, N)$ similar to the condition of the technique of PDM. Here, x_i is the observed magnitude at time t_i, we can estimate their mean $\overline{x}$ and the variance σ^2. Then we define a normalized periodogram for an angular frequency $\omega = 2\pi f > 0$ as follows,

$$P(\omega) = \frac{1}{2\sigma^2}\{\frac{[\sum_{i=1}^{N}(x_i - \overline{x})\cos\omega(t_i - \tau)]^2}{\sum_{i=1}^{N}\cos^2\omega(t_i - \tau)} + \frac{[\sum_{i=1}^{N}(x_i - \overline{x})\sin\omega(t_i - \tau)]^2}{\sum_{i=1}^{N}\sin^2\omega(t_i - \tau)}\}, \tag{2.11}$$

where the parameter τ is determined by the following equation,

$$\tan(2\omega\tau) = \frac{\sum_{i=1}^{N}\sin(2\omega t_i)}{\sum_{i=1}^{N}\cos(2\omega t_i)}. \tag{2.12}$$

Here, the parameter τ is the base time, phase 0, such that the result from equation (2.11) is equivalent to that from a least square fit for a given angle frequency ω.

Harris

Harris et al. [35] use the following equation to described the lightcurve variation of an asteroid,

$$H(\alpha, t) = \overline{H}(\alpha) + \sum_{l=1}^{m}\{A_l \sin\left[\frac{2\pi l}{P}(t - t_0)\right] + B_l \cos\left[\frac{2\pi l}{P}(t - t_0)\right]\}, \tag{2.13}$$

where $H(\alpha, t)$ is the computed reduced magnitude at phase angle α and time t, $\overline{H}(\alpha)$ is the mean absolute magnitude at phase angle α, A_l and B_l are Fourier coefficients, P is the rotation period, and t_0 is a zero-point time, chosen near the middle of the time span of the observations. In order to solve these parameters, we write the residual of the ith observation, $V_i(\alpha_j)$, from the above model,

$$\frac{\delta_i}{\varepsilon_i} = \frac{V_i(\alpha_j) - H(\alpha_j, t_i)}{\varepsilon_i}, \tag{2.14}$$

where α_j is the reference phase angle on the jth night and t_i is the time of the ith observation. ε_i is a prior error estimate of the ith observation.

A least square fit to equation (2.14) is found by finding the minimum of the bias corrected variance:

$$s^2 = \frac{1}{n-k} \sum_{i=1}^{n} \left(\frac{\delta_i}{\varepsilon_i} \right)^2 , \tag{2.15}$$

Where n is the total number of observations, $k = 2m + p + 1$ is the total number of free parameters of the solution, m is the degree of the Fourier series, and p is the total number of days of data, and the last "+1" is for the rotation period, also a solution parameter.

In comparison with the first two methods, Harris method can derive Fourier coefficients defining the shape of the composite light curve to any degree specified. In addition, a major advantage of the method is that it produces formal error estimates for all the quantities computed.

2.8.2 Planetary Phase Function

For airless bodies the light reflected from the surface interacts with a variety of surface structures composed of variety of particulates, large or small, transparent or opaque, and so on. Using measurements of the reflect solar light we attempt to measure the surface's compositions and physical properties. When our observations are taken in a series of phase angles from small to large ones, we can derive the ratio of its reflection or scattering to its illumination as a function of phase. The nature of this phase variation has been shown to probe both the nature of particles on the surface and the bulk structure of the surface [34].

Scattering models tend to link the surface property like roughness, material composition, and albedo with the scattering function, which describes the angular distribution of the reflected light. By analyzing the laboratory results of scattering of specific material we can draw a link between specific observations of the scattering function of an airless body and that body's surface composition. A phase function is a model that links the observations to the composition or a funcational parameterization that enables comparison of the surface compositions of groups of objects.

The phase function can consists of multiple parts. One part is the single-particle scattering phase function, and then two multiple scattering functions that describe the Shadow Hiding Opposition Effect (SHOE) and the Coherent Back-scattering Opposition Effect (CBOE). The SHOE and CBOE are physical explanations of the opposition surge effect where, for some materials, the brightness increases dramatically around zero phase angle.

In this work I will not be concerned with determining the precise physical parameters of 2002 MS4 phase function, but rather comparing the parameters with other airless bodies (asteroids and KBOs).

HG phase curves

HG system is a two parameter phase curve estimation adopted by the International Astronomical Union (IAU) to provide better estimations of magnitudes at different phase angles, especially at opposition as other models do not work well for predicting the opposition surge. The HG model is often used as a tool to estimate the absolute magnitude of a solar system object.

$$V(1,1,\alpha) = H - 2.5\log_{10}[(1-G)\Phi_1(\alpha) + G\Phi_2(\alpha)], \tag{2.16}$$

where, H is the mean absolute magnitude, which is the mean brightness for one revolution if an asteroid has a lightcurve. $V(1,1,\alpha)$ is the reduced visual magnitude at phase angle α. Here,

$$\Phi(\alpha) = (1-G)\Phi_1(\alpha) + G\Phi_2(\alpha)$$

is the integrated phase function if we assume a Lumme-Bowell scattering model. Φ_1 and Φ_2 are the single and multiple scattering phase function, respectively. G is the slope parameter and a smaller G means a darker surface and a larger G means a brighter surface. For asteroids, G is usually between zero and 0.5 [13]. When estimating H if no other evidence is known, $G = 0.15$ is usually assigned because it is the most likely G value for small bodies[68].

Bowell, Harris, and Lumme (1989) [2] came up with empirical forms of Φ_1 and Φ_2 for the integral phase functions. Their approximations (see equation (2.17) and (2.18)) are adopted by the IAU, valid for $0° \leq \alpha \leq 120°$ and $0 \leq G \leq 1$. Both of them are normalized such that $\Phi_1(0) = \Phi_2(0) = 1$.

$$\Phi_1 = \exp[-3.33\tan^{0.63}(\frac{\alpha}{2})] \tag{2.17}$$

---

[2] a manuscript that are often referred but unfortunately never published according to [68]

$$\Phi_2 = \exp[-1.87 \tan^{1.22}(\frac{\alpha}{2})] \tag{2.18}$$

2.8.3 The AB Phase function model

As we will find in the analysis of 2002 MS4's phase curve, the HG model, although the IAU adopted standard approach to representation of phase curves, does provide an acceptable parameterization. Shevchenko [70] proposes an alternative approach focuses on use of a simplified (fewer parameter) functional form that can accurately reproduce a large variety of phase curves:

$$V(1,\alpha) = V(1,0) - A/(1+\alpha) + B\alpha \tag{2.19}$$

Where $V(1,0)$ is the projected absolute magnitude, and A and B are constants fit to the phase curve observations. A characterizes the amplitude of the surge, and B characterizes the linear slope the large angle phase curve.

The Shevchenko model enables comparison of the surface properties of a variety of airless bodies using the minimal number of free parameters but does not provide any particular physical insight into physical properties of the surface. In this work I will determine the Shevchenko parameterization of 2002 MS4's phase curve to enable comparison of its surface composition to that of range of other bodies.

2.8.4 Phase Integral and Bond Albedo

The phase integral, q, is the weighted average of scattering over all phase angles. q is defined as

$$q = 2\int_0^{\pi} \Phi(\alpha)\sin(\alpha)d\alpha,$$

where $\Phi(\alpha)$ is the disk integrated reflectance normalized to unity at $\alpha = 0$. We can approximate q provided by Verbiscer & Veverka (1988) [89]

$$q \approx 0.135 + 2.671\Phi(70°),$$

where, $\Phi(70°)$ is the normalized reflectance at $\alpha = 70°$. The normalized reflectance is also referred to as the integral phase function. For an airless body this provides the brightness (radiant intensity) of the entire disk seen at some phase angle, α, divided by the brightness of its disk at $\alpha = 0°$. That is,

$$\Phi(\alpha) = \frac{I(\alpha)}{I(0)}$$

Using the phase integral and the measured geometric albedo one can determine the Bond albedo:

$$A_b = p_v q = \frac{\text{total radiated flux}}{\text{total incident flux}}.$$

Here, p_v is the geometric albedo and q is the phase integral. Brighter objects have larger Bond albedo and dimmer objects have smaller Bond albedo. The Bond albedo can be used to determine the temperature of the body and, form thermal flux observations, the size of the body can be determined.

2.8.5 The Hapke Model

The Hapke phase model attempts to describe the phase dependent scattering of light from physical principals[34]. Although not used in this thesis, a description of the Hapke model components provides some insight into the relation between phase curve observations and determination of the physical structure of a surface.

Single Particle Scattering Phase Function

The single particle scattering phase function describe the phase dependent relationship between incident wave and scattering wave for spherical particles with homogeneous refractive index. It is an imaginary model for perfect conditions but helpful as the first step on approaching more complex system. Hapke et al. [34] defines the particle phase function

$$Pi(\alpha) = \frac{4\pi I(\Omega)}{J\omega},$$

where Ω is the scattering outgoing solid angle, α is the phase angle, J is the incoming irradiance and ω is the particle single-scattering albedo, which is defined as the ratio of total power scattered to the total power removed from the wave. This particle phase function describes the angular scattering pattern of incoming power.

Multiple Scattering Phase Function

If a collimated light source is incident upon a medium of isotropic scattering, it is shown by Hapke [34] that the bidirectional reflectance is given by

$$r = \frac{w}{4\pi}\frac{\mu_0}{\mu + \mu_0}H(\mu)H(\mu_0) \tag{2.20}$$

where $H(x)$ is given by

$$H(\mu) = 1 + \frac{w}{2}\mu H(\mu)\int\limits_0^1 \frac{H(x)}{\mu + x}dx,$$

where $H(\mu)$ is recursive, so the exact solutions require numerical methods.

Opposition Surge

The opposition surge describes the effect of a large increment in the reflected light when observing an airless body near opposition (α approaches 0). Figure 2.7 demonstrates this phenomenon, in the figure we see a clear halo around the astronaut as he is pointing the camera to the Moon while the Sun is directly behind him. Theorists model the effect as combination of coherent back scattering effects (CBOE) and shadow hiding effects (SHOE).

Shadow-Hiding Opposition Effect The shadow-hiding effect happens when shadows are eliminated when both the incident angle and emission angle are around zero and therefore both the illumination shadows and the viewing shadows are minimized. The SHOE is a single-scattering phenomenon (valid when ω is small) and depends on the contrast of shadows with a media. However, if the surface is brighter (ω is large), then multiple scattering will tend to wash out shadows and reduce the magnitude of the effect.

Coherent Back Scattering Opposition Effects Coherent back-scattering opposition effect (CBOE) is the prominent contribution to the opposition surge when the planetary body has a high albedo and the multiply scattered light self interferes. In multiple scattering, the second scattered ray can travel the same path as the incoming ray but at a shifted phase. If the two rays constructively interfere the observed light intensity will increase. Figure 2.9 illustrates the light ray geometry causing the CBOE.

Figure 2.7: Opposition effect on moon. It is clear that we can see a bright halo around the photographer's head, where the phase angle is near zero.[51]

The phase difference $\Delta\phi$ between two rays is proportional to phase angle

$$\Delta\phi \approx 2\pi X \alpha cos\beta/\lambda,$$

where α is the phase angle (see Figure 2.9). When the phase angle is small, two light rays are more likely to coherently interfere and therefore the light intensity is quadrupled

$$|E_0 + E_0|^2 = 4E_0^2.$$

When the phase angle is large, the phase difference between two rays are more random and therefore the combined effect is the sum of two intensities,

$$|E_0|^2 + |E_0|^2 = 2|E_0|^2.$$

Hapke's model parameters

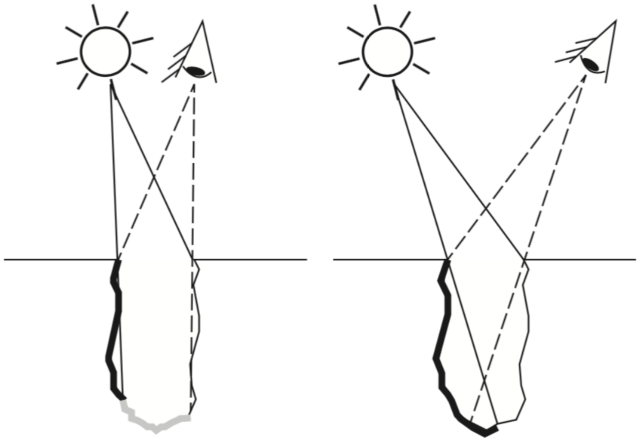

Figure 2.8: Shadow hiding opposition surge. Credit: Michael K. Shepard [68]

Hapke's photometric model is a complete description of scattering for unresolved planetary surface. The model provides us with a detailed expression about the composition particle character like the roughness. This completeness is achieved using 8 photometric parameters making Hapke's model most useful when there are a large number of observations over wide range of phase angels. The model itself is very complex so here we are only going to talk about the parameters referred in literature. Detailed model is included in the book by Hapke in 2012 [34].

- The single scattering albedo ω is the ratio of particle scattering efficiency and particle extinction efficiency. On the physical level, it relates to particle size, composition and micro-structure.
- Macroscopic roughness $\bar{\theta}$ represent the mean topological slope angle at resolution below pixel scale.
- Parameter b is from single particle phase function (SPPF) HG model. When $b > 0.5$, the compositing particles are regular and smooth; when $b < 0.5$, the particles are irregular and rough.
- Parameter c is from HG model as well. When $c < 0$, the compositing particles are more transparent; when $c > 0$, the compositing particles are more opaque. Both b and c are determined by the small and large phase angle data.
- h_s is the angular width of the inter-particle shadow hiding effect (SHOE). It represents the surface particle porosity and size distribution.

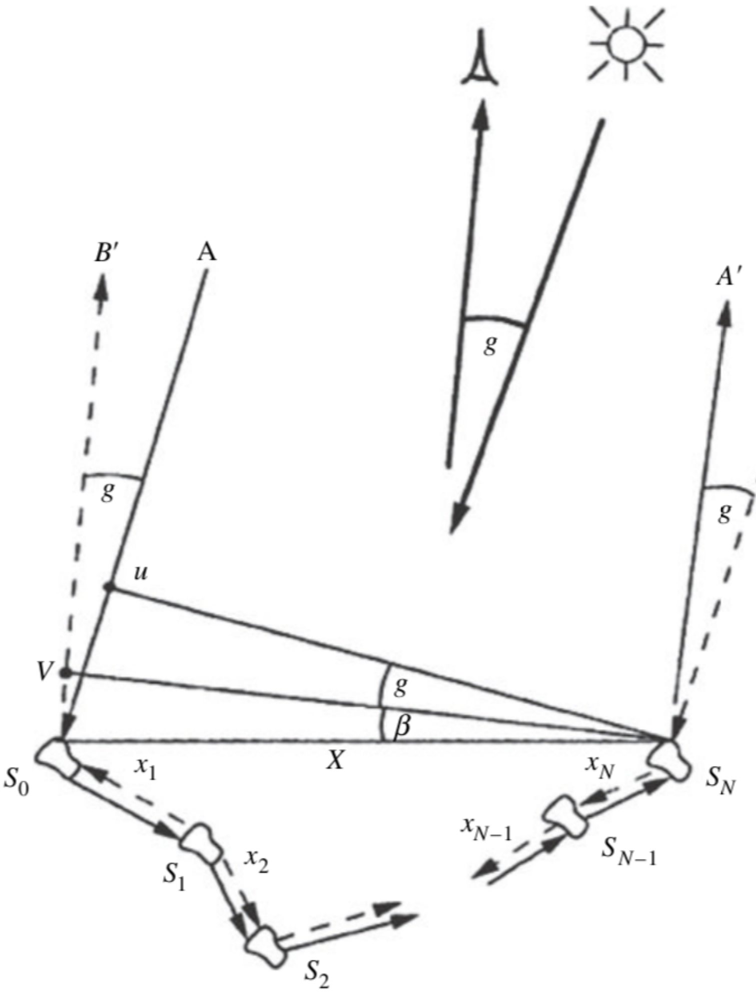

Figure 2.9: Light rays travel the same path but in reversed direction and constructively interfere. The interference decrease when the phase angle increase. Credit: B.Hapke [34]

- B_{os} is the amplitude of the SHOE and infers the particle transparency. When $B_{os} = 1$ the material is opaque.
- h_c is the angular width of coherent back scattering effect (CBOE). It is smaller than one rad. It depends on the the density and size of small scatters, which is related to the mean optical path length of photon.
- B_{oc} is the amplitude of CBOE and it is also smaller than unity. It is related to medium transparency.

Due to the sparseness of data available I do not attempt to model my phase observations using a Hapke model.

2.9 Stellar occultation

Using stellar occultation to determine the sizes of KBOs is relatively recent. The first stellar occultation by a KBO that was not Pluto was detected about 10 years ago [22]. Size and shape are basic physical parameters that must be accurately known if we want to fully characterize a target, and are the first step toward deriving other parameters. Stellar occultations provide a highly accurate probe of the size of these bodies and can even detect the presence of thin atmospheres. In combination with accurate brightness measurements, we can derive the body's geometric albedo which is indicative of the surface composition of the body. As mentioned in 2.7, the geometric albedo is also fundamental to analyzing the temperature and thermal behavior of the KBO. Although measurements of the thermal output of a solar system object can be used to obtain size and albedo, their accuracy will be much lower as they rely on assumptions about the emissivity and radiation beaming. A single chord observation across a body can be used to determine an estimate of the size of that body. If multiple occultation chords of the same event are observed then these can be used to derive an accurate size and shape of the object causing the occultation.

Stellar occultation is also powerful means to explore the presence of atmospheres when one observes a non-abrupt transition in the stellar brightness during the events of ingress and egress body or through the study of central flashes [56]. If the body causing the occultation is part of a binary system, then a total mass estimate is available and, when combined with the occultation-based size estimate, the bulk density of the KBO can be estimated. Lastly, the occultation technique can detect narrow and dense dust structures, such as rings around the KBO, through the dimming of stellar light[14, 57]. Figure 2.10 shows us the principle of stellar occultation.

The technique of the stellar occultation by KBOs provides a rich ensemble of data about the object but predicting the possibility of the even requires significant effort. First of all, the accurate prediction of an occultation event requires highly accurate positions for the occultated star and a very precise ephemeris of the KBO. Even the largest known dwarf planets, Eris and Pluto, subtends an angular diameter of only 0.03 arcseconds [72]. In other words, we require accurate positions as good as 0.03 arcseconds for both the occultated star and KBO. Historically, it is very difficult to obtain accuracy at this level. The situation has becomes more tractable thanks to

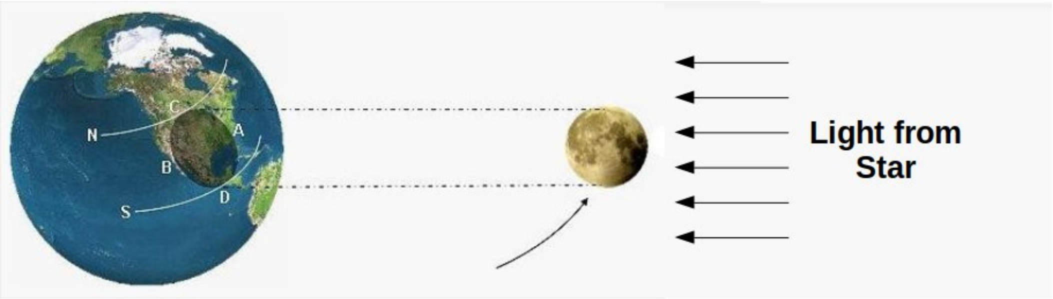

Figure 2.10: Illustration of a stellar occultation geometry. The light from a star is fully blocked in the shadow region on earth. Original source: IOTA, editted by G. Benedetti-Rossi.

the Gaia star catalogue (for example Gaia DR2 [15]). However, for a KBO, one must determine the orbit to high accuracy in order to achieve a position uncertainty of better than 0.03 arcseconds.

An alternative approach is to organize a large number of observers, including professional and amateur astronomers along a line that is perpendicular to the shadows path across the Earth, this is referred to as an occultation fence. Usually, the shadow path is in the East-West direction rather than in the North-South direction since the apparent sky motion of a KBO is dominated by the Earth's orbital motion. According to the statistics by Ortiz et al.[56], on average, the success rate in their occultation program is typically 1 every ~ 6 attempts when the occultation fence has a density of a few stations per expected size of the object and extends to cover the uncertainty in the shadow position. Here, a successful detection means a detection of the occultation from at least on site. Moreover, the number of participating stations is critical. Large campaigns involving at least 15-20 observing sites are typically needed to achieve multi chord observations.

In order to model the occultation event, a number of factors must be considered. I will give detailed expressions in the next section.

Using occultation chords we can estimate the size of the occulting body and determine a number of parameters, which can be combined with other observations, such as photometry at multiple phases, to obtain parameters that describe the physical surface of the KBO and place the object in the context of other small body populations of the solar system.

2.9.1 Geometric Occultation Light Curves

Following the practice of Elliot [22], we consider a square-well model of an occultation by a KBO without atmosphere. This model includes only the finite integration time of the data recording system and is based on geometric optics, so that the body's limb produces an abrupt cut off of the starlight. We define t_m as the occultation mid-time, T_d as the occultation duration, and Δt as the integration time of the data recording system. When the star is not occulted, the recorded full signal is s_f ,and when it is fully occulted, the recorded signal is s_b. If t_m is the mid-time of the i_{th} integration bin, then the recorded signal for that bin is $s(t_i)$. We can write equations for $s(t_i)$ for following five cases: (i) the integration bin lies completely outside the occultation, (ii) the integration bin lies completely within the occultation, (iii) the integration bin includes immersion, (iv) the integration bin includes emersion, and (v) the occultation lies completely within a single integration bin.

Specifically, if $t_i < (t_m - \Delta t/2) - T_d/2$ or $t_i > (t_m - \Delta t/2) + T_d/2$, then the integration bin lies completely outside of the occultation,

$$s(t_i) = s_f$$

If $t_i > (t_m + \Delta t/2) - T_d/2$ and $t_i < (t_m - \Delta t/2) + T_d/2$, then the integration bin lies completely inside of the occultation, then

$$s(t_i) = s_b$$

if $t_i > (t_m - \Delta t/2) - T_d/2$ and $t_i < (t_m + \Delta t/2) - T_d/2$, then the integration bin straddles immersion, then according to liner interpolation

$$s(t_i) = s_f \left[\frac{(t_m - T_d/2) - (t_i - \Delta t/2)}{\Delta t} \right] + s_b \left[\frac{(t_i + \Delta t/2) - (t_m - T_d/2)}{\Delta t} \right]$$

If $t_i > (t_m - \Delta t/2) + T_d/2$ and $t_i < (t_m + \Delta t/2) + T_d/2$, then the integration bin straddles emersion, then according to liner interpolation

$$s(t_i) = s_b \left[\frac{(t_m + T_d/2) - (t_i - \Delta t/2)}{\Delta t} \right] + s_f \left[\frac{(t_i + \Delta t/2) - (t_m + T_d/2)}{\Delta t} \right]$$

if $t_i > (t_m - \Delta t/2) + T_d/2$ and $t_i < (t_m + \Delta t/2) - T_d/2$, then the integration bin contains the full occultation event, then

$$s(t_i) = s_b \left[\frac{\Delta t - T_d}{\Delta t}\right] + s_f \left[\frac{T_d}{\Delta t}\right]$$

The duration of the event can then be determined via minimization of the χ^2 between the piece wise light curve described above and the observed flux from the stellar source. Once the duration of the event has been determined the size of the object can be estimated using the sky-position ephemeris to determine the velocity across the line of sight and the duration of the event. The diffraction fringes will not be discussed in this thesis as the object scale is large enough and SNR of the time series is low such that the diffraction pattern power is indistinguishable from the background noise[65].

Size Estimation

For objects larger than about $D > 500$ km we can anticipate that an icey body will take on a shaped that is in hydro-static equilibrium. Nominally, two classed of shapes are considered, A Jacobi-ellipsoid ($a > b > c$) and a MacLaurin-ellipsoid ($a = b > c$) [21]. For my observations however I have only two chords and a sensible assumption for $2002MS_4$, which is expected to have $D > 500$ km, is that the object is spherical (a=b=c). A more complete analysis considering a MacLaurin surface is left to a future work.

With the spherical shape assumption, the occultation shadow cast on the Earth is circular and the chord duration provides an estimate of the diameter of the body. My goals is to determine the most likely diameter of a spherical object from a set of uncorrelated observed chords. Each chord is a random draw across the circular shadow cast by the object. Figure 2.11 illustrate the circle with radius r and chord length D. D can be anywhere in the circle and we can use angle θ and radius r to represent D.

To find the average length of the chord D_{avg}, we can write equation

$$D_{avg} = \frac{1}{\pi}\int_0^\pi 2\,r\sin(\theta)\,d\theta$$

and get

$$D_{avg} = \frac{4r}{\pi} \tag{2.21}$$

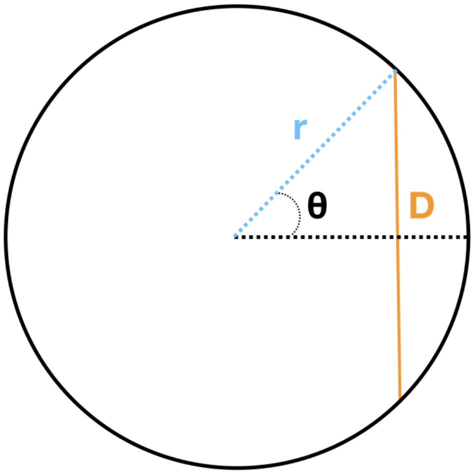

Figure 2.11: Illustration of an occultation chord (D) crossing at an arbitrary location across a circular shadow of radius r.

rearranging the equation gives,

$$r_{avg} = \frac{D_{avg}\pi}{4} \tag{2.22}$$

In other words, if we find the average chord length D_{avg}, we can find the most likely radius of the circle r_{avg} and therefore the most likely radius of the KBO assuming it is spherical.

Chapter 3

The Phase Curve

The Kuiper belt object *2002* MS_4 (also MS_4) has Keplarian heliocentric orbital elements a=47.17 au; e =0.14; i=17.7^o (see Figure 3.1) and is classified as a member of the 'hot component' of the classical Kuiper belt. Objects in this zone of the solar system are thought to have formed closer to the Sun, perhaps in the 15-20 Astronomical Unit (au) zone, and been scattered to their current locations via dynamical interactions with the giant planets. This is in contrast to those Kuiper belt objects on lower-inclination nearly circular orbits that appear to have formed in situ. The interior formation zone contained sufficient material to allow the formation of the dwarf planet population of the Kuiper belt prior to their transport into this zone; there are no 'large' Kuiper belt objects within the low-inclination population. I report detailed on the photometry of MS_4 based on observations from the Canada-France-Hawaii Telescope (CFHT) MegaCam, and the New Horizons LORRI, cameras.

Precise photometry for KBOs is performed using a large (> 2 m) aperture telescope due to the faintness of the objects. These photometric measurements are most often reported in the Johnson-Cousin $UBVRI$ standard photometric system [e.g. 80, 69, 85]. Those authors have used strict procedures to derive precise photometry. For example, a few standard stars in Landolt 1992 [49] are observed each night to calibrate and an optimal aperture is adopted to make photometry. The requirement of large apertures, strict observing procedures, and photometric observing conditions have limited the availability of phase curve observations.

Our photometry for MS_4 via the archival observations of the CFHT/Megacam is very different. And its data reduction is also different. It is impossible for us to go back in time and use the telescope to observe some standard stars in the Landolt system on the same night as our archive data. Our archive data can, however, be

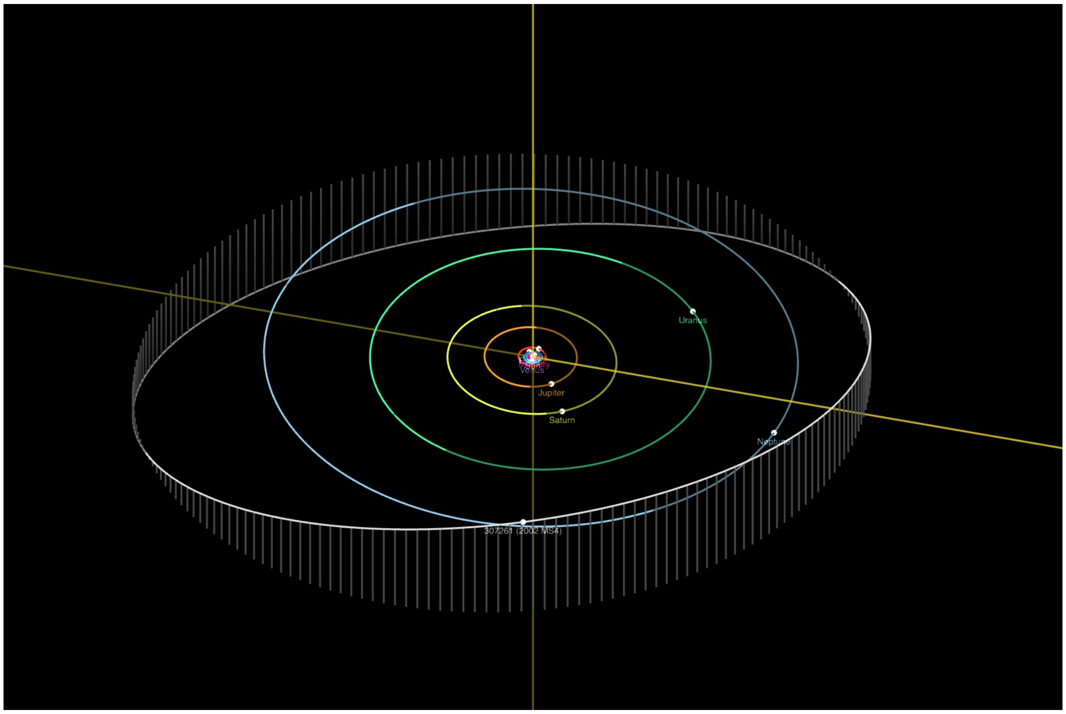

Figure 3.1: The orbit of *2002* MS_4 (white curve) compared to Jupiter (innermost ring), Saturn, Uranus, and Neptune.

calibrated using stars in the image that have calibrated fluxes provided by the PanSTARRS projects. We use the in-place calibrated stars to compute a zero-point for the natural CFHT/Megacam photometric system to measure the photometry of MS_4 . We then use well-known calibration curves. provided by the Canadian Astronomy Data Centre's MegaPipe service [32], to convert from the CFHT/MegaCam system to the SDSS photometry system.

I also report observations obtained with the LORRI camera onboard the New Horizon spacecraft (see 2.1 for details). The LORRI photometric observations were obtained at large solar phase angles (only possible because the spacecraft is observing the Kuiper belt from within the Kuiper belt). Using the LORRI data we obtain phase angle coverage for the MS_4 that can not be obtained by Earth-localized observation. Note that all observation on MS4 are non-resolved.

The next section will detail the photometry of MS_4 obtained using CFHT/Megacam from their original images to the final standard magnitude. In section 3, the photometry of MS_4 from the New Horizon Spacecraft is reported. The final section provides a parametric representation of the observed phase curve.

3.1 CFHT Photometry

3.1.1 Data Discovery

Owing to the brightness of the target MS_4 has been observed frequently and the heliocentric orbit is well determined. I utilized the Canadian Astronomy Data Center (CADC) Solar System Object Image Search tool (SSOIS)[1] [33] to locate archived observations of the target.

SSOIS provides a user-friendly way to search for images of objects whose celestial coordinates change with time Images of moving objects in the archives can be obtained by searching by object name and SSOIS then uses one of the Lowell Observatory or Minor Planet Centre or Jet Propulsion Laboratory (JPL) ephemeris services to cross-match the ephemeris of the target with a catalog of imaging data. I limited my search to CFHT's MegaCam (see Figure 2.3) observations instrumentally detrended and calibrated data are available for that facility. The CFHT images have been processed through the CFHT Elixir[2] system to remove the signal pattern of the telescope/detector system (bias subtracted and flat-fielded)

---

[1] https://www.cadc-ccda.hia-iha.nrc-cnrc.gc.ca/en/ssois/

[2] https://www.cfht.hawaii.edu/Instruments/Elixir

and basic robust photometric and astrometric calibration has been performed with the relevant information present in the FITS image header. The CFHT data found by my SSOIS search and used in the subsequent analysis are listed in Table 3.1.

Table 3.1: Raw CCD frames of MS_4 from CFHT/MegaCam.

image_ID	Date/time	Filter	Exp time(s)
1635849p00.fits	2013-07-04 11:12:50	r	45
1635850p09.fits	2013-07-04 11:14:33	r	45
1635851p00.fits	2013-07-04 11:16:10	r	45
1635852p00.fits	2013-07-04 11:18:06	r	45
1635853p00.fits	2013-07-04 11:20:23	r	45
1635854p00.fits	2013-07-04 11:21:56	r	45
1635856p00.fits	2013-07-04 11:25:15	r	45
1635857p01.fits	2013-07-04 11:26:59	r	45
1636059p00.fits	2013-07-05 10:00:03	r	45
1636072p00.fits	2013-07-05 11:47:10	r	45
1636073p01.fits	2013-07-05 11:48:43	r	45
1636074p10.fits	2013-07-05 11:50:16	r	45
1636075p13.fits	2013-07-05 11:51:50	r	45
1636076p13.fits	2013-07-05 11:53:23	r	45
1636077p12.fits	2013-07-05 11:54:56	r	45
1636078p12.fits	2013-07-05 11:56:29	r	45
1636079p13.fits	2013-07-05 11:58:03	r	45
1636080p13.fits	2013-07-05 11:59:36	r	45
1636081p16.fits	2013-07-05 12:01:10	r	45
1636082p17.fits	2013-07-05 12:02:59	r	45
1636083p13.fits	2013-07-05 12:10:52	r	45
1636084p13.fits	2013-07-05 12:12:25	r	45
1636185p16.fits	2013-07-06 10:49:49	r	45
1636187p17.fits	2013-07-06 10:53:17	r	45
1636188p17.fits	2013-07-06 10:54:50	r	45
1645301p22.fits	2013-08-03 10:10:15	r	45
1645516p22.fits	2013-08-04 08:59:22	r	45
1645517p22.fits	2013-08-04 09:00:55	r	45
1645518p22.fits	2013-08-04 09:02:29	r	45
1645519p22.fits	2013-08-04 09:04:20	r	45
1645520p22.fits	2013-08-04 09:05:53	r	45
1645522p22.fits	2013-08-04 09:09:00	r	45
1645846p22.fits	2013-08-06 09:24:50	r	45
1645847p22.fits	2013-08-06 09:26:23	r	45
1645848p22.fits	2013-08-06 09:27:56	r	45
1646190p22.fits	2013-08-08 08:06:14	r	45
1646191p22.fits	2013-08-08 08:07:54	r	45
1646192p22.fits	2013-08-08 08:09:27	r	45
1646378p22.fits	2013-08-09 08:08:24	r	45
1646379p22.fits	2013-08-09 08:10:04	r	45
1646380p22.fits	2013-08-09 08:11:37	r	45

3.1.2 Astrometric Calibration

A Flexible Image Transformation System (FITS) file is an array of data and each array element is called a pixel, referring to the physical CCD pixel of the detector. Each pixel has its own unique integral position (x, y) in the array and each element's value is proportional to the number of photons detected at that image location. Usually, the size of an image is the field of view, such as 1024 × 1024. FITS is the standard format for the storage and exchange of CCD images [31]. The mapping of pixel array locations in a FITS image to the celestial sky coordinate is referred to as the World Coordinate System (WCS) of the image. For our MS_4 image, I performed astrometric calibrations to precisely map each pixel position to a sky location.

I used the program `SExtractor` [8] to detect and obtain the pixel position of the stellar sources in the image. I then selected sources between 16 and 21 magnitudes (based on the Elixir zero-point in the header) as reference stars. Stars in this magnitude range were selected as that is the range available from our astrometric reference catalog. SExtractor provided the centroid, magnitude, and magnitude error for each source to be used as input into my astrometric calibration.

I used the stars selected from Gaia DR2 [15] as the reference for stellar positions (RA, DEC). The selected Gaia star and SExtractor positions were input into the MegaPipe `dofit` astrometric program [33]. `dofit` converts the source (x, y) pixel position into (RA, DEC) using Elixir World Coordinate System (WCS) and then conducts a course matching between the Gaia and Elixir catalogs. (In some cases, I consulted a sky-map using the Aladin tool [11] and manually selected a new initial WCS `dofit` program to start with as the Elixir software did not always provide a useful starting point.) Using the matched list `dofit` then computes a new WCS of increasing complexity (order) until a convergent WCS is obtained. The WCS is represented as a linear component (CRVAL, CRPIX, CD) that describes the tilt, rotation, and offset of each CCD compared with the sky plane; and a set of polynomial terms (PV) that describe distortions in the projection of the curve sky onto the flat CCD imager. In most cases, `dofit` successfully matched 300-500 sources and return a WCS with an uncertainty of < 0.005 arcseconds.

`dofit` provides the WCS polynomials in PV format [see 33] which I converted to the SIP standard [71] such that the WCS can be interpreted correctly by `astropy` package. Once the WCS is corrected, I determined the (RA, DEC) of MS_4 at the time when the image was taken (using the JPL ephemeris service) and visually identify MS_4 on the image. I then extracted a 500 × 500 sub-image centered on the location of *2002* MS_4 . When MS_4 was less than 250 pixels from the edge of the image array, I shifted the sub-image centre such the sub-image would still be 500 × 500.

I also selected a set of images of the region of the sky where MS_4 had been imaged but at a time when MS_4 was not present. These 'blank' images were processed similarly to the MS_4 -containing images. The blank images are used to supplement the data available for image differencing.

3.1.3 Difference Image

The observer's line of sight to *2002* MS_4 is transiting the galactic plane, and the field is significantly crowded with stars. See figure 3.2 for a sample image demonstrating the crowded nature of the images. We apply a difference-imaging technique prior to photometric measurement to remove the background variations caused by the stellar crowding. For my analysis, difference-image comes in handy as all the background objects are stationary while the KBO is moving. After performing the difference-imaging, only the KBO will remain while all background stars are subtracted. I utilized the ISIS [1, 2] difference image package for this analysis. The ISIS software package minimizes the difference between a convoluted reference image and the target image by optimizing a convolution kernel, a linear combination of basis functions. The resulting difference image (target image - convoluted reference image) is an impressively clean subtraction of background stars, leaving just the moving target object.

3.1.4 Aperture Photometry

Aperture photometry assumes that all point source profiles in a given image are the same. For a well-designed optical reflecting telescope, the point source function's (PSF's) core is well represented by a Gaussian, while the extended zone is consistent with a Moffat function, this form is known as a King profile [47]. Specifically, the general star profile can be represented by the following equation

$$S(r; R_i, A, B, C, D) = B \cdot M(r; A) + (1 - B)[C \cdot G(r; R_i) + (1 - C) \cdot H(r; D \cdot R_i)], \quad (3.1)$$

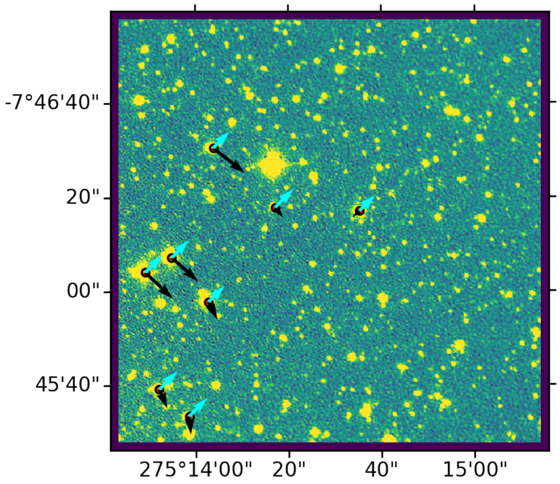

Figure 3.2: *2002 MS_4* in a crowded stellar field, obtained with CFHT MegaCam.

where

$$G(r;R_i)=\frac{1}{2\pi R_i^2}\exp\frac{-r^2}{2R_i^2},$$

and

$$M(r;A)=\frac{A-1}{\pi}(1+r^2)^{-A},$$

and

$$H(r;D\cdot R_i)=\frac{1}{2\pi(D\cdot R_i)^2}\exp\frac{-r}{D\cdot R_i},$$

where G is a Gaussian profile represent the core, M is a Moffat profile represent the aureole and H is the exponential function connecting two profiles smoothly. Unfortunately, this function has many free parameters, and fitting this function to the light profile from a faint source profile will result in a highly uncertain determination of the parameters. We can, however, take advantage of the fact that all point sources have the same profile and determine the value of the shape from bright sources and only use the faint source to determine the normalization.

I follow the growth curve aperture photometry method described by [78]. This method measures the total flux of a source while achieving a maximal signal-to-noise ratio (SNR) when measuring faint sources. The flux of a number of bright stellar sources is measured through a series of k concentric apertures, and the

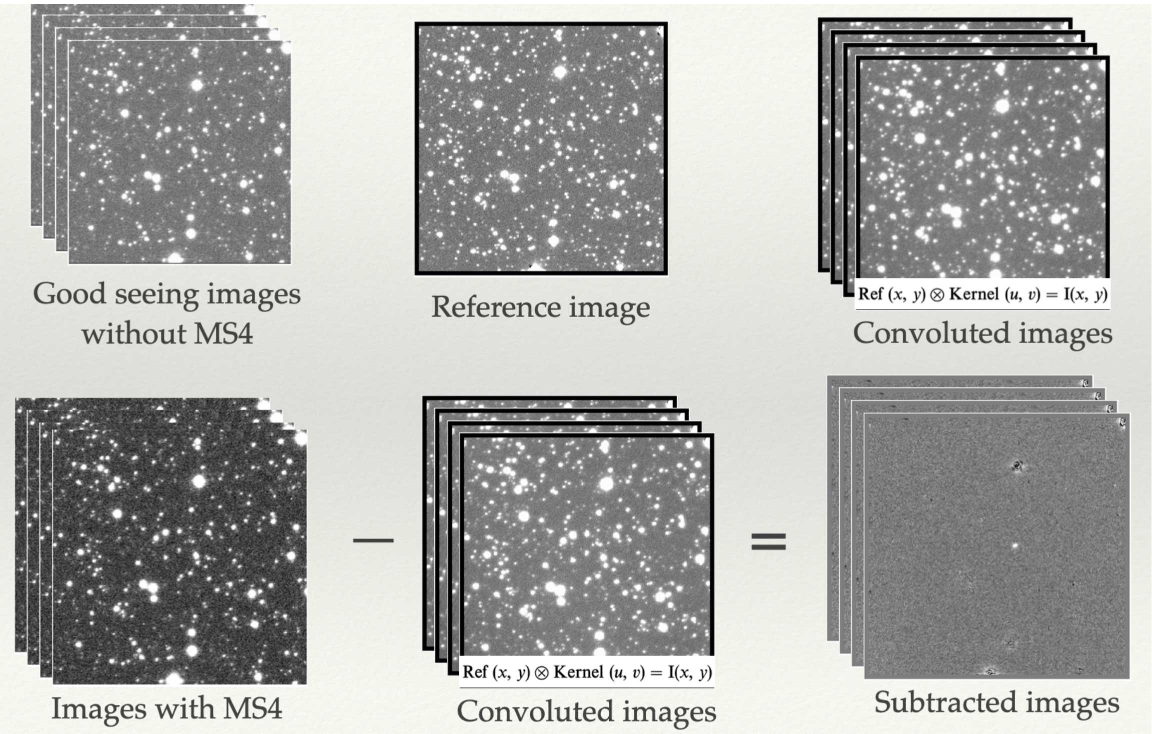

Figure 3.3: Illustration of how ISIS package removes all stars other than MS4 in the image.

magnitude difference, δm_k, between each consecutive aperture is computed. If we plot the δm_k of all the apertures as a function of aperture radius, we get the 'growth curve' of the source. Figure 3.4 is a sample of a single growth curve. The growth curve is a representation of the stellar PSF sampled by the different sources. I then find, via least-squares fitting, the best match between the growth curve and the ratios of King profiles integrated to the same series of the apertures as in the growth curve, i.e., the measured δm_k is approximated with the profile

$$\Delta m_k = -2.5 \log[\frac{\int_0^{r_k} S(r; R_i, A, B, C, D)(2\pi r)dr}{\int_0^{r_{k-1}} S(r; R_i, A, B, C, D)(2\pi r)dr}]$$

and the best fit values of the parameters R_i, A, B, C, D are determined. The King's profile parameters are fit, via least-squares, to a collection of growth curves of 10-15 bright stars per CCD frame. The bright stars are chosen such that they don't have bright neighbours, and their dim neighbours are removed by repeatedly building a PSF of stars of the frame and subtracting those sources, using the `IRAF\verb`PSF and `SUBSTAR`routines, until the sky is smooth around the chosen bright stars. The

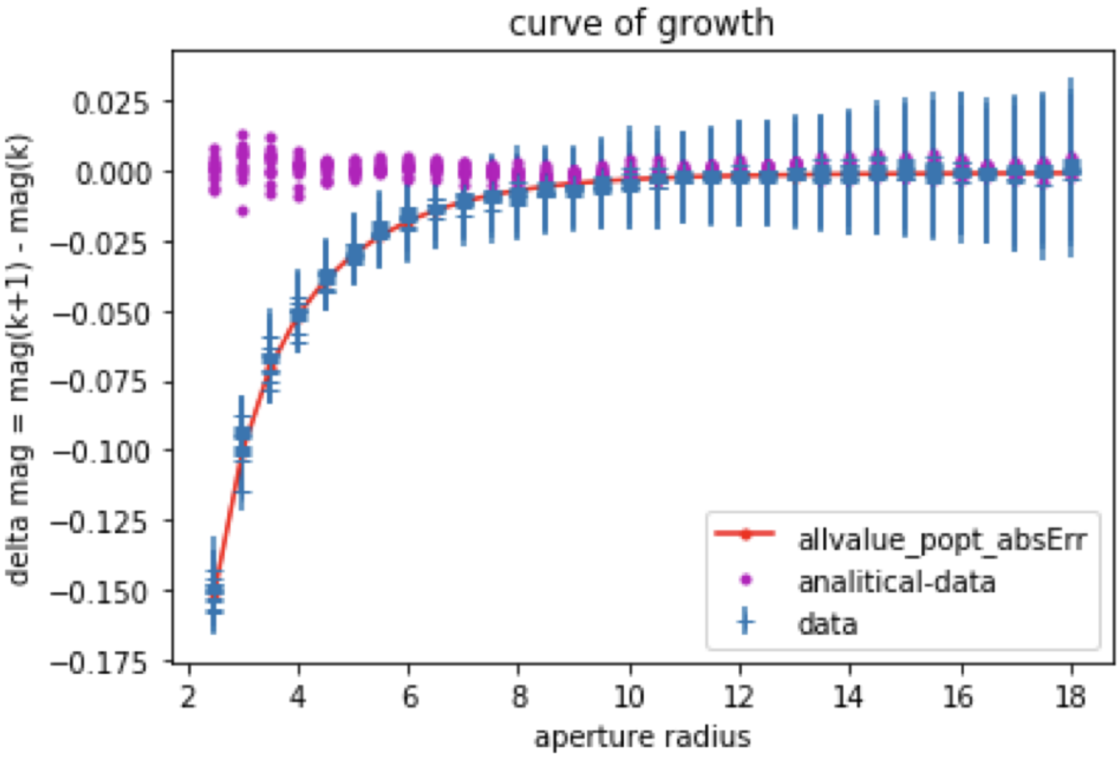

Figure 3.4: A sample curve of growth. Magnitude at 5 FWHM is given by magnitude at 1.1 FWHM plus the Aperture Correction Value. And the Aperture Correction Value equals to the sum of delta(k) for k range from 1.1 to 5 FWHM

procedure mentioned above will reduce the influence of the neighbour stars on the sky value, reducing the uncertainty in the measured flux. Then with the best-fit king's profile parameter, we can construct a best-fit curve of growth and sum up the Δm_k from an aperture that is 1.1 times the FWHM to 5 times FWHM. This summed flux between a large and small aperture,

$$\text{ApCorr} = \sum_{k=1.1FWHM}^{5\times FWHM} \Delta m_k$$

is the aperture correction value. The final magnitude of the source will be the magnitude at 1.1 times the FWHM plus the aperture correction value. The uncertainty in the final flux is taken as the quadrature sum of the uncertainty in the small aperture magnitude and the uncertainty from the aperture correction value (as determined via the least-squares fit).

3.1.5 Photometry from CFHT/Megacam

The Canada-France-Hawaii Telescope Megacam (CFHT/Megacam) in $R.MP9601$ pass-band observations (hereafter referred to as r) is closely matched to the SDSS r' and was used to obtain the photometry of MS_4 reported here. I make my flux measurements in the natural photometry system of CFHT/Megacam using well-measures stars within the image to determine the zero point. The CFHT/Megacam (g, r) magnitudes differ slightly from the SDSS scale [33]. However, to enable comparison between objects, the photometry of a source, like a KBO, must be reported in some standard photometry system, such as UBVRI or SDSS *ugriz* (see Chapter 2). Here, I calibrated the CFHT/MegaCam measured magnitudes to the SDSS *ugriz* system due to the CFHT/Megacam photometry system's similarity to the standard SDSS photometry system.

The images containing *2002* MS_4 do not contain any reference stars for the SDSS *ugriz* system and no contemporaneous standard star observations were available in the CFHT MegaCam archive. Thus direct calibration was not possible. In addition, the SDSS survey had not observed the field where *2002* MS_4 was standard, excluding the possible use of SDSS-calibrated observations. However, the fields containing *2002* MS_4 are located in an area that the PanSTARRS project had observed. Using the PanSTARRS flux catalogue [23] I tied our CFHT MegaCam observations to the PanSTARRS system. Those PanSTARRS catalogue r magnitudes were transferred to the CFHT MegaCam system using the calibration curves published on the CADC website [3]

$$r_{Megacam} = r_{PS} + 0.002 - 0.017 \times (g - r)_{PS}$$

(ignoring higher-order terms). Where $r_{Mwegacam}$ is the magnitude of a source measured in the MegaCam system and r_{PS} and $(g - r)_{PS}$ are the magnitude and colour index in the PanSTARRS system

In summary, the PanSTARRS source magnitudes are converted CFHT MegaCam, and those CFHT MegaCam magnitudes are used to calibrate my images. The magnitude of *2002* MS_4 is then computed using aperture-corrected photometry and calibrated to the CFHT MegaCam system using per frame zero points determined using the PanSTARRS reference stars. The *2002* MS_4 CFHT MegaCam magnitude is then transformed to the SDSS standard photometry system using the

---

[3] http://www.cadc-ccda.hia-iha.nrc-cnrc.gc.ca/en/megapipe/docs/filt.htm

transformation equations published on the CADC web site:

$$r_{SDSS} = r_{Megacam} + 0.024 \times (g - r)_{SDSS}.$$

To use this transform requires knowledge of the color of MS4 in the SDSS system. The Johnson-Cousin (JC) colour index of *2002* MS_4 is $(R - V) = 0.38 \pm 0.02$ and $(B - V) = 0.690 \pm 0.020$ [79] and $(g - r) = (1.646 \times (V - R) - 0.139) \pm 0.005$ [45] such that $(g - r)_{MS4} = 0.49 \pm 0.02$. Combining the measured colour of MS4 with the MegaCam to SDSS transform above gives

$$r_{SDSS} = r_{Megacam} + 0.024 \times 0.48 = r_{Megacam} + 0.01 \pm 0.02.$$

For targets with the colour *2002* MS_4 , the two filter systems are very well matched. Table 3.2 lists the apparent magnitudes of MS4 from CFHT/MegaCam calibrated to the SDSS system. In the table σ is the estimated standard deviation based on the propagation of the measurement uncertainty and does not include the systematic uncertainty in the system transformation (±0.02 mag), MJD0 is the beginning time for each CCD frame exposure, r is the distance from our target to the Sun and Δ is the distance to the Earth, both in units of AU, *phase* is the solar phase angle in degrees, and *zpt* is the photometric zero point.

3.2 Rotational Light Curve

In order to solve a possible rotation light Curve, there are three major steps we follow. First, we remove the phase coefficient effect. Second, we solve for a possible period of the light curve. Third, we construct a phase function from the fluxes with light curve variation removed and redetermine the phase coefficient. Finally we redetermine the rotational light curve period.

3.2.1 Remove Phase Coefficient Effect

It is well known that the opposition effect usually exists for a KBO in observations taken at a small phase angle ($\alpha < 2$ °). Following [e.g. 62, 40] we first estimate the phase effect to find the phase-corrected magnitude of the source and then determine a rotation period of our target. Specifically, we first determine the raw reduced magnitude by removing the variation due to changes in the distance of MS_4 and the *zpt* in Table 3.2 based on the measured apparent magnitude.

Table 3.2: Apparent magnitude *mag* from CFHT/MegaCam of MS4 in the SDSS system.

MJD0	r_{SDSS}	σ	Δ_{au} (AU)	r_{au} (AU)	$phase_{deg}$ (deg)	zpt	$instr.$
56477.4669852	19.186	0.018	46.024	46.996	0.367	-0.933	MegaCam
56477.4681877	19.210	0.016	46.024	46.996	0.367	-0.933	MegaCam
56477.4693028	19.183	0.018	46.024	46.996	0.367	-0.933	MegaCam
56477.4706523	19.220	0.021	46.024	46.996	0.367	-0.933	MegaCam
56477.4722338	19.188	0.017	46.024	46.996	0.367	-0.933	MegaCam
56477.4733095	19.176	0.018	46.024	46.996	0.367	-0.933	MegaCam
56477.4756161	19.172	0.017	46.024	46.996	0.367	-0.933	MegaCam
56477.4768169	19.176	0.017	46.024	46.996	0.367	-0.933	MegaCam
56478.4919056	19.178	0.016	46.026	46.996	0.376	-1.009	MegaCam
56478.4929841	19.177	0.017	46.026	46.996	0.376	-1.009	MegaCam
56478.4940691	19.200	0.017	46.026	46.996	0.376	-1.009	MegaCam
56478.4951483	19.193	0.019	46.026	46.996	0.376	-1.009	MegaCam
56478.4962281	19.187	0.018	46.026	46.996	0.376	-1.009	MegaCam
56478.4973079	19.241	0.017	46.026	46.996	0.376	-1.009	MegaCam
56478.4983929	19.204	0.017	46.026	46.996	0.376	-1.009	MegaCam
56478.4994692	19.204	0.017	46.026	46.996	0.376	-1.009	MegaCam
56478.5005531	19.152	0.018	46.026	46.996	0.376	-1.009	MegaCam
56478.5018152	19.187	0.017	46.026	46.996	0.376	-1.009	MegaCam
56478.5072935	19.206	0.017	46.026	46.996	0.376	-1.009	MegaCam
56478.5083721	19.236	0.018	46.026	46.996	0.376	-1.009	MegaCam
56479.4510102	19.205	0.019	46.028	46.996	0.385	-0.983	MegaCam
56479.4520882	19.202	0.018	46.028	46.996	0.385	-0.983	MegaCam
56479.4534087	19.190	0.018	46.028	46.996	0.385	-0.983	MegaCam
56479.4544851	19.193	0.018	46.028	46.996	0.385	-0.983	MegaCam
56512.3374019	19.364	0.025	46.249	46.990	0.851	-0.986	MegaCam
56512.3385587	19.312	0.032	46.249	46.990	0.851	-0.986	MegaCam
56512.3396390	19.284	0.026	46.249	46.990	0.851	-0.986	MegaCam
56535.3443763	19.360	0.016	46.544	46.986	1.111	-0.993	MegaCam
56535.3454544	19.312	0.017	46.544	46.986	1.111	-0.993	MegaCam
56535.3561390	19.399	0.013	46.544	46.986	1.111	-0.993	MegaCam
56535.3572188	19.390	0.016	46.544	46.986	1.111	-0.993	MegaCam
56602.1936835	19.320	0.060	47.570	46.975	0.960	-0.991	MegaCam
56602.1947633	19.269	0.056	47.570	46.976	0.960	-0.991	MegaCam
56919.2215853	20.205	0.016	46.751	46.920	1.211	-0.122	MegaCam
56919.2232999	20.163	0.015	46.751	46.920	1.211	-0.122	MegaCam
56922.2194877	19.342	0.018	46.800	46.919	1.218	-0.956	MegaCam
56922.2212075	19.324	0.016	46.800	46.919	1.218	-0.956	MegaCam

Figure 3.5 shows the raw reduced magnitude against the solar phase angle. A straight line with slope β is used to approximate the relationship between the reduced magnitude and solar phase angle. We then remove the effect of phase

coefficient β by the following equation,

$$m(1,\alpha) = m(r,\Delta,\alpha) - 5 \times \log_{10}(r \times \Delta) - zpt - \beta \times \alpha \tag{3.2}$$

where $m(r,\Delta,\alpha)$ is the *mag* in Table 3.2, r is the distance from the Sun to MS_4 and Δ is the distance from the observer to MS_4 in unit of au, and α is the solar phase angle in degrees. Using the uncertainty-weighted linear least squares parameter estimation, β_i is 0.16 ± 0.02 mag/deg and the $\chi^2_{dof} = 7.22$. Although this χ^2 indicates that the linear curve does not represent the observed relation well, this approach enables a first-pass removal of the phase effect such that the light-curve can be determined.

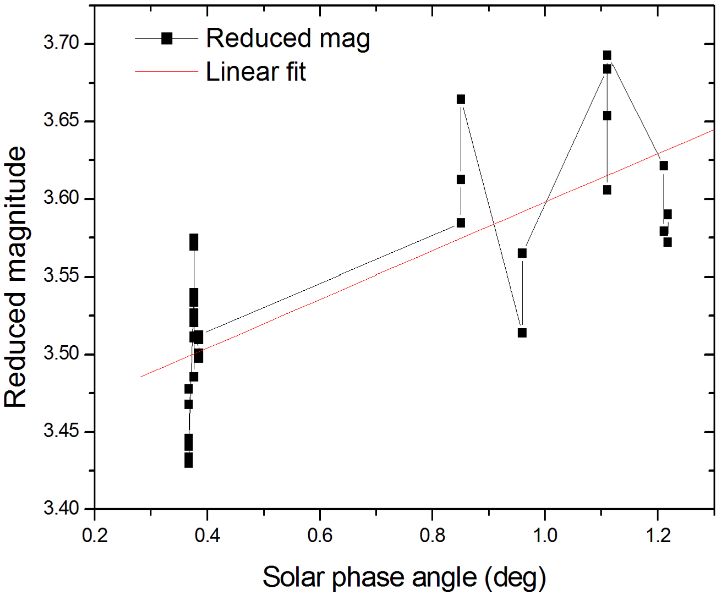

Figure 3.5: Phase coefficient is found by fitting the reduced magnitude using a straight line.

3.2.2 Solve for a Possible Period of Lightcurve

In order to obtain an accurate period of lightcurve of MS_4 , I need a precise time record of light starting from MS_4 ; I correct the $MJD0$ in Table 3.2 to account for the light-travel time difference due to the different observer/target circumstances in our archive data. I first compute the mid-exposure time since the beginning of the exposure. The exposure time is 45s for all frames and I add half of that to $MJD0$. Then I need the light travel time from the MS_4 to the observer so that we know the MS4-centric mid-exposure time to compute the lightcurve period (1 AU $\sim$ 499.0047815 light seconds). After both corrections are made to $MJD0$, I obtain MJD, which is the mid-time of light emission in the MS_4 reference frame. The MS_4 time-tagged reduced magnitudes can then be used to measure possible light-curve effects.

Due to a limited number of observations available, it is not convenient to use the Phase Dispersion Minimization algorithm[73] to compute the period. Instead, I use the Lomb algorithm modified by Press [61] to solve for periods. I use trial periods between 4 to 21 hours, the normalised periodogram P(ω) is shown in Figure 3.6. The three most probable trial periods in Figure 3.6 are $T_1 = 14.251h, T_2 = 8.932h$ and $T_3 = 5.881h$. T_1 has the largest spectral power and thus is the most probable rotation period. The Lomb algorithm assigns confidence greater than 99.3% that this signal is non-random (i.e., periodic).

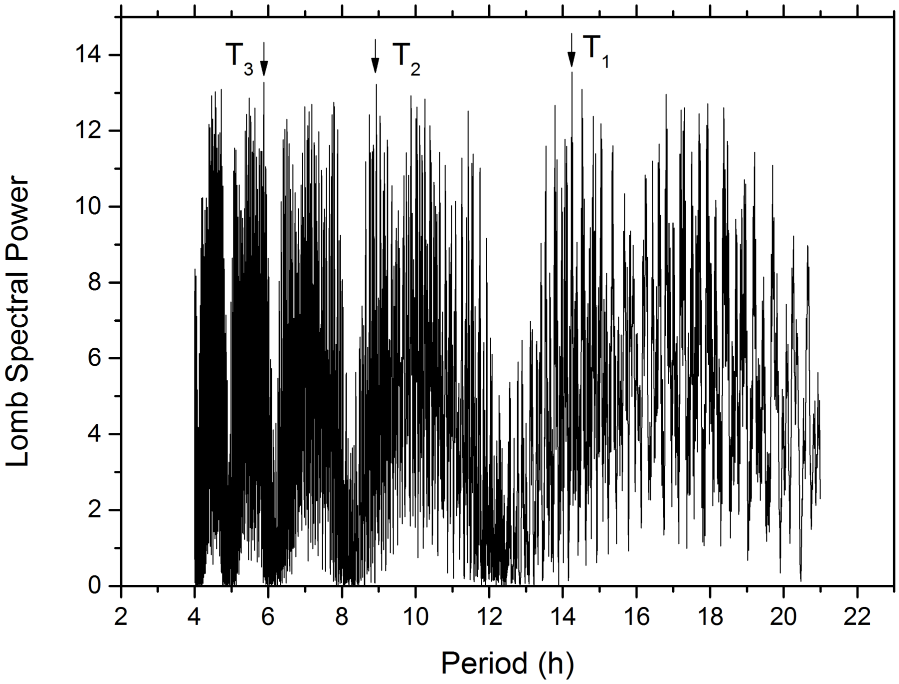

Figure 3.6: Normalized periodogram of trial periods by Lomb algorithm. Here three periods are possible: T_1=14.251 h, T_2=8.932 h and T_3=5.881 h.

Using the most probable period T_1 I fit the following equation to the reduced magnitudes.

$$m(1,0) = c + a\sin(\omega t) + b\cos(\omega t), \tag{3.3}$$

where $\omega = 2\pi/T_1$ and time t is the mid light emission time in the MS_4 reference frame (MJD in Table 3.2). Parameters a, b and c are determined by least square fit,

$$c = 3.437 \pm 0.004, a = -0.030 \pm 0.005, b = -0.050 \pm 0.004.$$

Giving $\chi^2 = 56.87$ and χ^2 per degree of freedom, $\chi^2_{dof} = 1.67$.

3.2.3 Recursively Computing the Rotational Phase Function

I adopted a recursive data rejection process to constrain the rotational light-curve and phase function better. First, I compute the normalized residuals by dividing the light-curve fit residual for each point by its estimated uncertainty. From the normalized residual distribution (see Figure 3.7 left panel) I determine the width of the residual distribution and identify as outliers and observations more than 3 standard deviations from 0. I remove the outlier point (there was only one) from the data set and recompute the phase and rotation curves. I find $\beta = 0.17 \pm 0.01$ for the new solar phase coefficient after removing the raw rotational light curve effect (i.e., as in equation 3.3) and the outlier point is removed. I then remove the phase curve and recompute the rotation period. This recursive process result in a new periodogram. Fortunately, the newly solved most possible rotational period keeps the same ($T_{1new} = 14.251h$). I then fit to equation 3.3 again and obtain a new set of parameter values as follows for the rotational light curve:

$$c = 3.435 \pm 0.003, a = -0.029 \pm 0.005, b = -0.054 \pm 0.004.$$

The right panel of Figure 3.7 shows the new residual distribution. The dispersion of the new reduced magnitude is considerably smaller than their first distribution and is more consistent with a normal distribution. In addition, the goodness of fit is substantially improved with $\chi^2_{dof} = 1.33$ compared to 1.67 prior to the iterative rejection process. The rotational phase function over two periods is presented in Figure 3.8

The distribution of reduced magnitudes with solar phase is shown in Figure 3.9

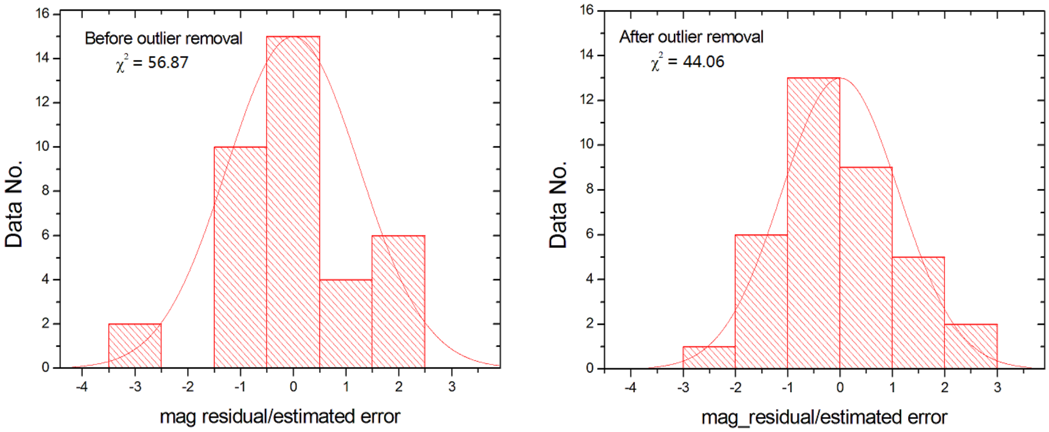

Figure 3.7: Normalized residual distribution for the case $T_1 = 14.251$ hr.

before and after the removal of the rotational light curve. The goodness of phase effect linear fit before and after rotation curve removed χ^2_{dof} improved significantly from the originally 7.22 to 1.33 (both have the outlier point removed).

3.3 Photometric Data from New Horizons

3.3.1 New Horizons

Hew Horizons was launched in 2006 with its mission to explore the Pluto system and the Kuiper Belt. In July 2015, New Horizons explored Pluto's surface, atmosphere, and satellites with resolved images [74]. The extended mission phase began in 2016 with the goal to explore Kuiper Belt Objects [76]. The most well-known target of the extended mission is the close fly-by of the cold classical KBO 2014MU_{69} at the beginning of 2019. The spacecraft gathered measurements of the physical properties of MU_{69} including its flattened shape, albedo heterogeneity, and the presences of discrete geological units [77, 95].

In addition to the close fly-by, the LOng Range Reconnasiance Imager (LORRI) on the spacecraft (a clear filter imager) observed ∼25 distant KBOs, Centaurs, and dwarf planets [75]. Specifically, LORRI distant observations had the following goals:

- determine the shape, rotation rates, and pole positions by light curves at multiple aspect angles;
- search for ring and dust materials with high-phase photometry;

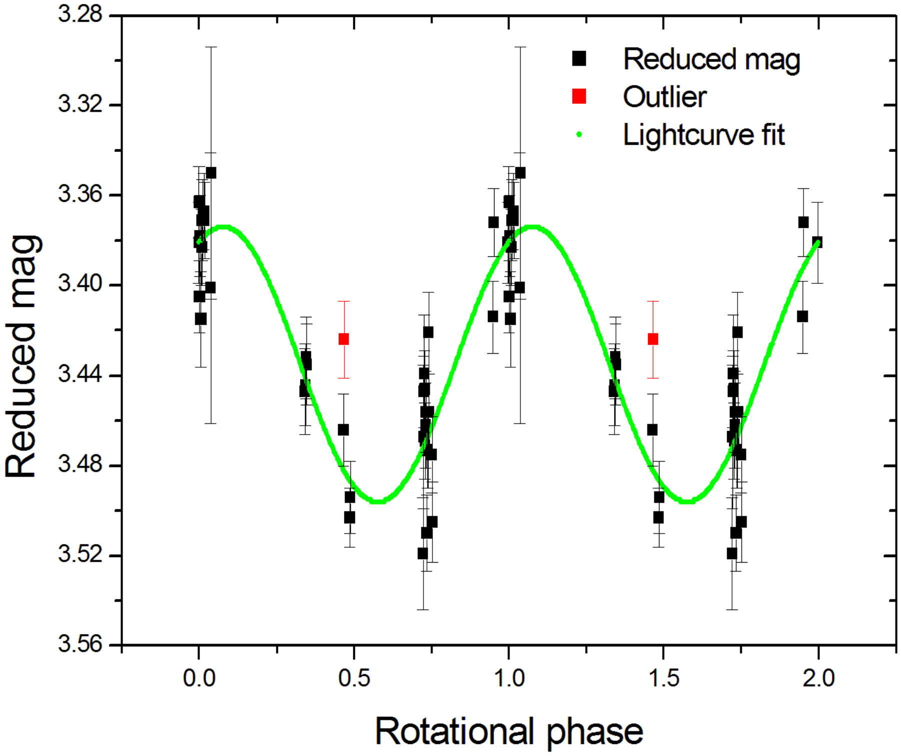

Figure 3.8: Light-curve of *2002* MS_4 folded at 14.251 h and shown for two periods. The same data is shown twice to better illustrate the rotation curve; typically presentation for asteroid rotation curves. The dark squares represent the reduced magnitudes with 1-sigma error bars and the red square is the one rejected measurement. The green line is the final light curve.

- refine KBO's orbits by performing high-parallax astrometry;
- determine phase functions and regolith microphysical properties by photometry at moderate and high phase angles;
- search for small satellites and closer binaries.

3.3.2 Photometry of MS4 by New Horizons LORRI

The high phase observation Of MS_4 were obtained by New Horizons LORRI ([18, 93] and Section 3.3). The bandpass of this clear imager extends from 350nm to 850nm with a pivot (central) wavelength of 601nm. The reduction technique to deliver the photometry of LORRI is described in [60] and was carried out by the

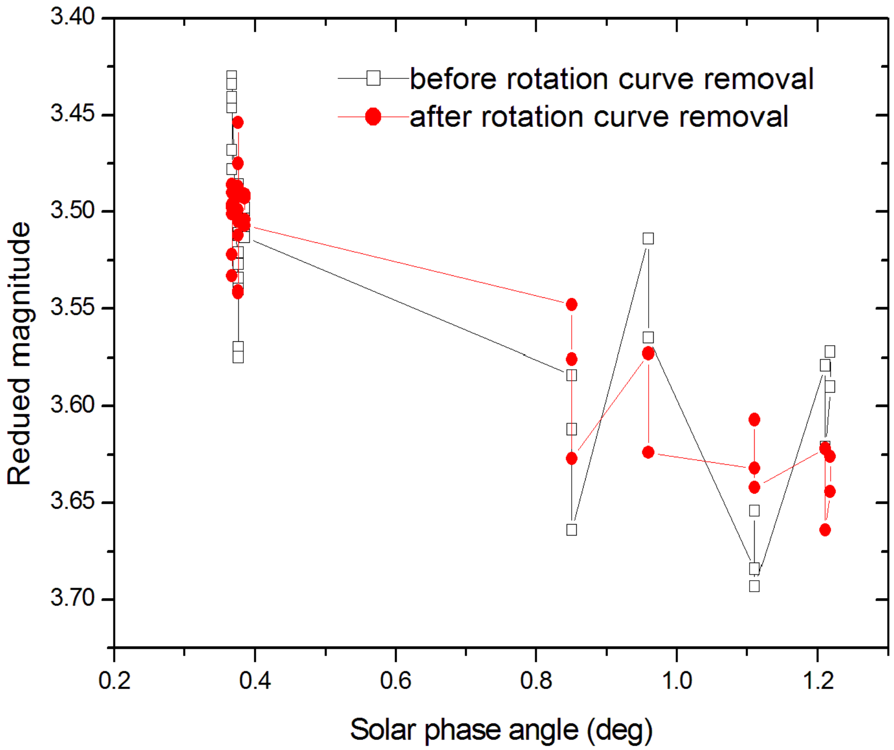

Figure 3.9: Phase curve for the observations of CFHT/MegaCam before and after MS4's rotational curve is removed. The open squares represent the reduced magnitude before the removal and the red point is for the reduced magnitude after the removal without error bars for clarity. Here, the outlier is not displayed.

LORRI distant TNO team. The clear filter LORRI observations are tied to $UVCRI$ system using a transformation equation derived by observing a series of Landolt stars [60]:

$$V = -2.5\log_{10}(DN/s) + 18.94 + CC \tag{3.4}$$

where DN/s is the data number per second and CC is a colour correction term. As reported above, the colour index for MS_4 is ($V - R = 0.38 \pm 0.02$) which is similar to the solar value over the LORRI bandpass (350 nm to 850 nm) resulting in CC=0 for this source [93]. The high-phase flux measurements from New Horizons combined with the CFHT MegaCam r observations (prior to light-curve correction) were presented in [88] and are reproduced in Table 3.3 . As my photometry of MS_4

using CFHT MegaCam is represented in SDSS r AB magnitudes, I first transform those values to Johnson V magnitude for inclusion with the New Horizoins high-phase observations. We use the calibration from [27] for this transformation:

$$r = V - 0.84(V - R) + 0.13$$

Apply the $V - R$=0.38 colour of MS_4 , giving $V = r + 0.189$.

Table 3.3: New Horizons LORRI flux measurements of *2002* MS_4 .

year mon day	hh mm ss.sss	Δ (AU)	r (AU)	*phase* (deg)	*mag*	*err*	*instr.*
2016 07 13 15	02 30.243	15.339	46.799	37.777	19.725	0.199	LORRI
2016 07 14 07	32 30.243	15.336	46.798	37.794	19.369	0.142	LORRI
2017 10 31 00	02 04.720	13.256	46.706	51.392	19.802	0.237	LORRI
2017 11 01 00	02 04.721	13.252	46.706	51.424	19.758	0.331	LORRI
2017 11 02 00	02 05.722	13.249	46.706	51.457	19.532	0.189	LORRI
2019 09 01 20	36 30.385	12.006	46.570	76.207	20.024	0.201	LORRI
2019 09 02 21	52 30.386	12.005	46.569	76.249	19.954	0.186	LORRI
2019 09 04 15	47 30.388	12.005	46.569	76.317	20.027	0.203	LORRI

3.4 Phase curve of MS4

I transformed all observations from CFHT and New Horizons to reduced magnitudes (i.e. removed the observer and Sun distance components using Equation 2.2) and those values are presented in Table 3.4. In the table, the light curve variation has been removed from the CFHT magnitudes however, the New Horizons values are not corrected for rotation. The observations from New Horizons are rather dispersed and obtained at large phase angles where the rotation light curve may be quite different. For all observations reported in Table 3.4 the MJD values are in the MS_4 centric frame.

The reduced magnitudes versus solar phase angle of observations are shown in Figure 3.10. The magnitude values at low phase angle are from the CFHT MegaCam data and are the average values at each phase angle (Figure 3.9 presents the individual measurements), while the high phase angle values are from New Horizons.

Table 3.4: Reduced V magnitude of MS4 for all observations.

MJD	*phase* (deg)	*Vmag* (mag)	*err* (mag)	MJD	*phase* (deg)	*Vmag* (mag)	*err* (mag)
56477.2014332	0.367	3.687	0.018	56479.1878336	0.385	3.680	0.018
56477.2026357	0.367	3.711	0.016	56479.1889100	0.385	3.682	0.018
56477.2037508	0.367	3.684	0.018	56512.0705504	0.851	3.816	0.025
56477.2051003	0.367	3.722	0.021	56512.0717072	0.851	3.765	0.032
56477.2066818	0.367	3.690	0.017	56512.0727875	0.851	3.737	0.026
56477.2077575	0.367	3.679	0.018	56535.0758210	1.111	3.796	0.016
56477.2100641	0.367	3.675	0.017	56535.0875837	1.111	3.831	0.013
56477.2112649	0.367	3.679	0.017	56535.0886635	1.111	3.821	0.016
56478.2263420	0.376	3.664	0.016	56601.9192025	0.960	3.813	0.060
56478.2274205	0.376	3.664	0.017	56601.9202823	0.960	3.762	0.056
56478.2285055	0.376	3.688	0.017	56918.9518345	1.211	3.853	0.016
56478.2295847	0.376	3.681	0.019	56918.9535491	1.211	3.811	0.015
56478.2306645	0.376	3.676	0.018	56921.9494539	1.218	3.833	0.018
56478.2317443	0.376	3.730	0.017	56921.9511737	1.218	3.815	0.016
56478.2328293	0.376	3.694	0.017	57582.5381482	37.777	5.445	0.199
56478.2339056	0.376	3.694	0.017	57583.2256656	37.794	5.089	0.142
56478.2349895	0.376	3.643	0.018	58056.9248832	51.392	5.843	0.237
56478.2362516	0.376	3.679	0.017	58057.9249064	51.424	5.800	0.331
56478.2417299	0.376	3.701	0.017	58058.9249353	51.457	5.574	0.189
56478.2428085	0.376	3.731	0.018	58727.7893441	76.207	6.286	0.201
56479.1854351	0.385	3.696	0.019	58728.8421277	76.249	6.217	0.186
56479.1865131	0.385	3.693	0.018	58730.5886555	76.317	6.290	0.203

3.4.1 HG Model Fit

To compare the MS4 photometry with other KBOs, we model our photometry as a function of solar phase angle with a least squares fit to the IAU standard two-parameter system, which is the HG magnitude system [13] (see in Section 2.8.2.

$$V(1,1,\alpha) = H - 2.5\log_{10}[(1-G)\Phi_1(\alpha) + G\Phi_2(\alpha)] \tag{3.5}$$

where, H is the mean absolute magnitude, $V(1,1,\alpha)$ is the reduced visual magnitude at phase angle α. Φ_1 and Φ_2 are the single and multiple scattering phase function, respectively (see Equations 2.17 and Equations 2.18.

Figures 3.10 and 3.11 present the reduced Johnson V magnitude with respect to the solar phase angle and a least-squares best fit to the HG model. I find that best fit model curve results in an absolute magnitude of $H = 3.614 \pm 0.013$ and slope

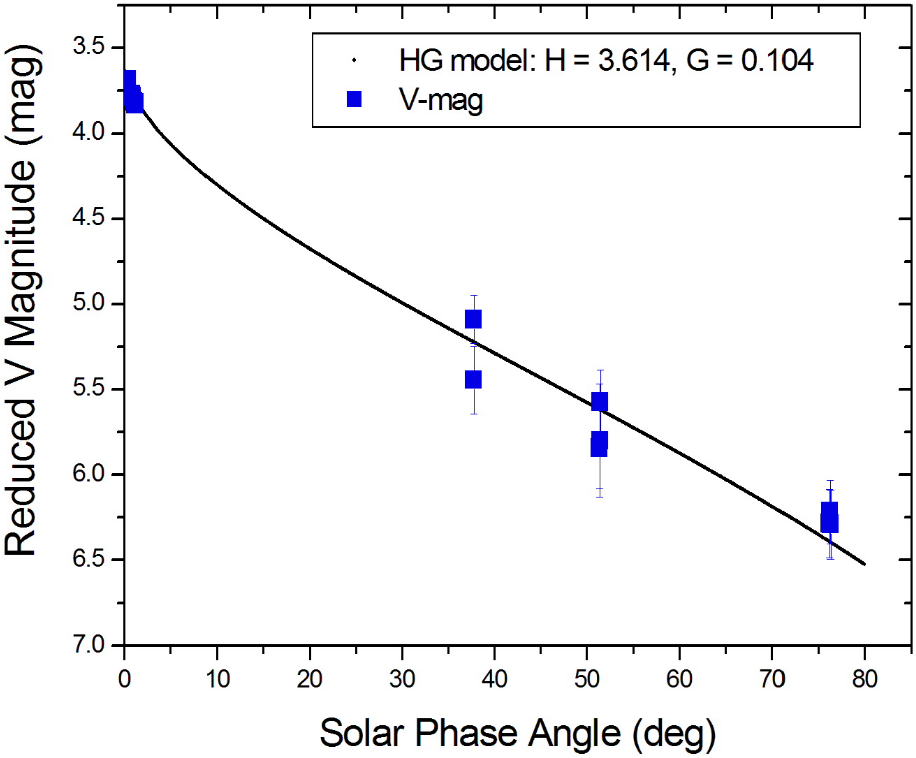

Figure 3.10: *2002* MS_4 HG phase curve for $\alpha < 80^o$. The blue points are the reduced magnitudes, where the CFHT values are averages at the given phase angle and rotation light-curve effects have been removed. The solid line is the best-fit model.

parameter of $G = 0.104 \pm 0.013$. Figure 3.11 clearly demonstrates that the standard IAU approved phase model does not provide an acceptable representation of the observations.

3.4.2 Shevchenko AB Phase Curve Model

Though we have valuable observations MS4's reduced magnitude values measured over a wide range of phase angles is not well matched to the HG model. As described in Section 2.8.3 the Shevchencko AB model provides an alternative representation. The three-parameter empirical model propose by Shevchenko [70] (see Equation 2.19) provides a very good approximation of asteroid phase curves. Interestingly, this model is found to also provide an acceptable parameterization of

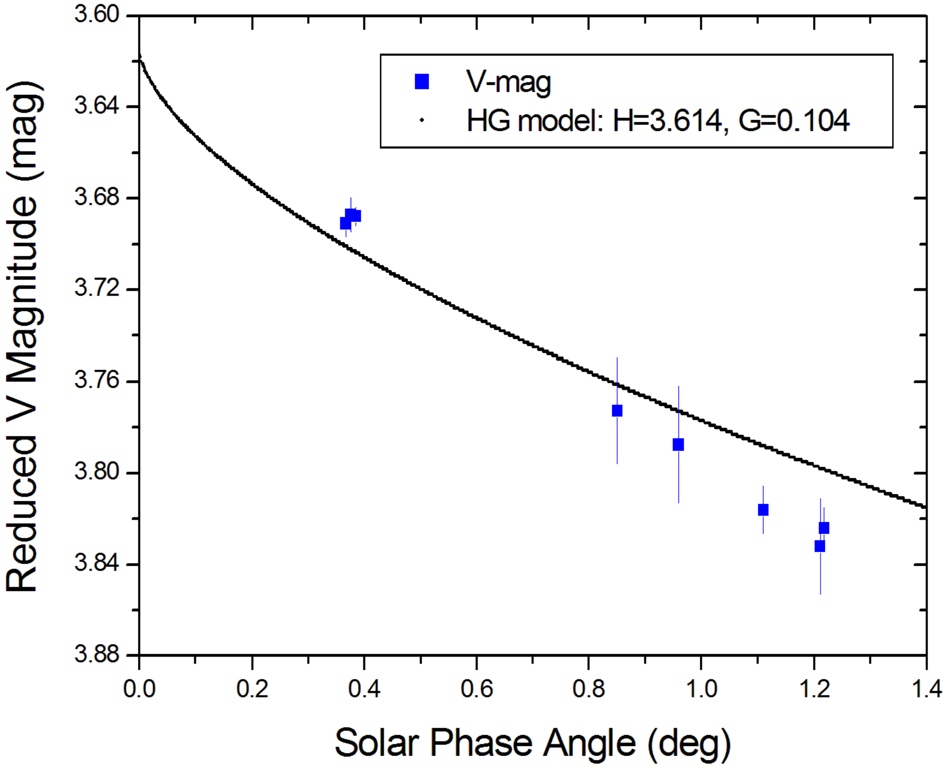

Figure 3.11: 20002 MS4 HG phase curve from $\alpha < 1.5^o$. (see Figure 3.10 for details)

2002 MS_4 's phase curve.

Figure 3.12 shows my *2002* MS_4 observations compared to the AB phase model. In the large phase range, the AB model curve is similar to that of the HG model, at small angles, however, at small phase angle the AB model is significantly better than HG model. $\chi^2_{dof} = 1.19$ for the AB model, which is satisfactory and much better than that of HG model. In fact, Belskaya and Shevchenko [5] found that the HG model is usually not a good model and as it fails to accurately describe the phase behaviour for asteroids of high and low albedo. My fit parameters by equation 2.19 are,

$$V(1,0) = 3.977 \pm 0.018, A = 0.414 \pm 0.026, B = 0.031 \pm 0.001.$$

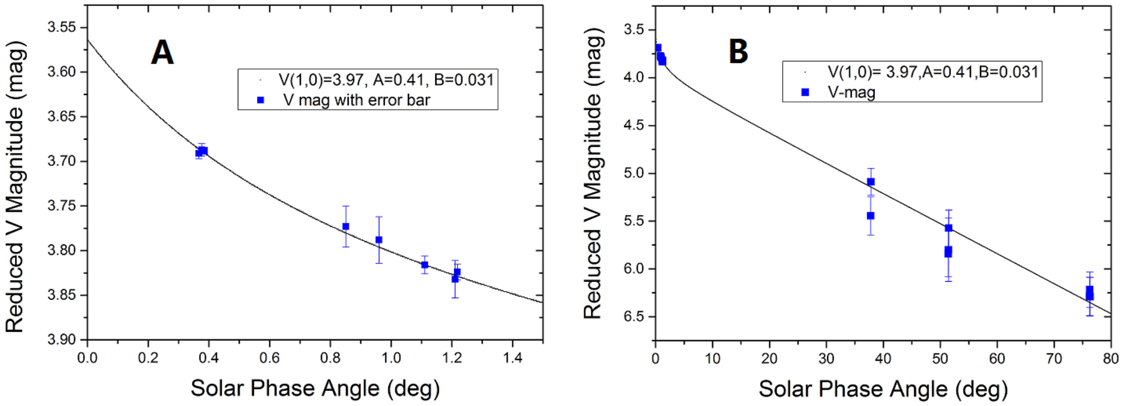

Figure 3.12: *2002* MS_4 AB phase curve. Panel A: $0^o < \alpha < 1.5^o$. Panel B: $0^o < \alpha < 80^o$ S. (see Figure 3.10 for details)

The absolute magnitude is then determined using these best-fit parameter values

$$H_V = V(1,0) - A = 3.56 \pm 0.03$$

The difference between the absolute magnitudes derived from HG and AB models is approximately 0.05 magnitude (5%) while the χ^2_{dof} prefers the AB model. I adopt the AB model derived absolute magnitude $H_V = 3.56 \pm 0.03$ to be the absolute magnitude of 2002 MS4.

3.4.3 Opposition Surge

I have found no evidence of an opposition surge for MS4. There is a possibility that for low albedo bodies, a surge may exist at a very narrow phase angle below 0.1 - 0.2 degrees [6] as the observations reported here do not cover these very small phase angles. Achieving very low-phase observations requires observation when the object passes through its node (i.e. is aligned with the ecliptic plane). Unfortunately, *2002* MS_4 passed through its node in about 1954 and will not do so again until 2103. It is left to future generations to determine if MS4 exhibits an opposition surge.

Chapter 4

Occultation Events

4.1 Introduction

As described in Section 2.9, and occultation event can be used to determine the size of asteroid or KBO. One determines the size by measuring the duration of the occultation event, time between the ingress (start) and egress (end), combined with knowledge of the relative motion between the Earth and occultor. The timing/velocity combination provides the length of a 'chord' across the remote object, when we treat the background star as a stationary point source, a reasonable approximation for the geometries considered here. The length of an individual chord provides a measure of the minimum size of the object. In this chapter I present the determination of the chord length across 2002 MS4 for two occultations events observed from Anarchist Mountain in BC Canada.

4.2 The Events

Two occultation events were observed on two separate nights, 2020-Jul-26 and 2020-Aug-19, both observed from the same location. The observations took place as part of an observing campaign organized by the Lucky Star project.[1] Both nights' data were acquired at the Anarchist Observatory. The Anarchist Observatory regularly conducts occultation observations as part of the Research and Education Collaborative Occultation Network(RECON)[2]. The obsevatory is located at latitude +49.008827 degree, longitude -119.362968 degree and 1087 m elevation. Observations were acquired using a QHY174m-GPS imager. The QHY camera uses a CMOS detector with 1920 × 1200 pixels and a 1 ms readout time without

---

[1] https://lesia.obspm.fr/lucky-star/index.php

[2] http://tnorecon.net/

mechanical shutter. The QHY camera has an integrated GPS receiver enabling accurate (better than 1ms) absolute time resolution. The images were stored directly as FITS image files and tagged with the GPS time of start of the integration. Details of the observational system are reported in Table 4.1.

Table 4.1: Anarchist Mountain Observatory

Optical Layout	Maksutov-Cassegrain Astrograph Telescope
Mirror-Diameter	30 cm
f/#	4.9
camera	QHY174M-GPS
effective scale	0.8 arcseconds/pixel
image size	1920×1200
field of view	26.3×16.5 arcminutes
effective gain	0.067 e^{-1}/ADU
readout noise	2.3 e^{-1}

The line of site to 2002 MS4 currently has the disk of the Milky Way in the background and the object frequently occults the line of sight to background disk stars. Two predicted occultation events were observed, one with a predicted central time of 2020-0726T10:15:12Z and the other at 2020-08-19T07:36:30Z. We obtained 88 usable images spanning the July-26th event and 66 spanning the time of the August 19th event, with sampling times of 2 s and 4 s.

Similar to the technique we use in Chapter 3 for data from CFHT MegaCam, I perform image subtractions on the set of images to be at the same photometric zero points and remove the flux from non-variable sources. For each set of frames, I first identify the occulted star and extracted a small sub-frame (500 × 500 pixels) around the occulted star. I then stacked the sub-frames using the ISIS simple-stack procedure (average with 3-sigma pixels values clipped). This stacked template image was then used to subtract the static sky from the individual exposures with the resulting images normalized to a uniform flux zero point. I then use the Python package `photutils`, a `astropy` sub-package, to perform aperture photometry on the occulted star in the static-sky subtracted images. The stellar flux was measured in a circular aperture with a radius of 1.1 times the FWHM of the seeing, which achieves a maximum S/N ratio for a Gaussian Point Spread Function (PSF)[37]. After measuring the flux, I constructed a time-series view (a.k.a. light-curve) of the measured flux against the mid-time of each frame. In this light-curve we see a noticeable dip (see Figure 4.1) in the flux from the star, at the time of the predicted occultation by 2002 MS4.

To determine the duration of the occultation event I fit a square well model to the time-series observations. To fit to the square well model described in Section 2.9 we first re-normalize the data so that the average flux level during the occultation is zero and outside the time of the event the average flux is unity. The square-well model is a five parameter function that models the occultation event light curve as a constant flux prior to and after the event with a monotonically decreasing, then flat, and then increasing flux during the ingress, event, and egress. See equations in Section 2.9 for a description of the model parameters. I used the `curve_fit` module of the `scipy` Python package which implements a *least squares* approach to estimate the best fit parameters for the piece-wise square well model function given our time-series observations. Table 4.2 summarizes all four parameters as determined by least squares parameter fitting for the two occultation events while Figure 4.2 displays the flux from the occulted star and the corresponding square well fit.

Table 4.2: Parameters of square well for occultation data

Obs Date	T_d(s)	t_m(s)	s_f	s_b
2020 July 26	35.054±0.544	94.379±0.259	1.015	0.030
2020 August 19	33.802±1.023	88.036±0.512	1.020	-0.070

Using the two observed chords I provide an estimate of the size of MS4. To derive the size of of a SSO (Solar System Object) via occultation requires a minimum of one chord. Multiple chords of the same event can be combined together to provide a measure of the shape of the occultor as the chord lenghts from different sites essentially map out the objects shadow on the Earth. With two chords we can compute an average estimate of the size of the occultor.

My data set contains the measurement of two unique chords observed from the same site but from two different occultation events. One can not use these two events to uniquely derive the diameter of MS_4 as the ephemeris uncertainty in the sky location of 2002 MS4 is large and the relative geometry the chords across the surface can not be determined with sufficient accuracy. Even so, we can compute two chord lengths for MS_4 and compare those two values as independent estimates of the minimum size of the object. Table 4.3 lists the two chord lengths in terms of the ephemeris' speed in the sky-plane. I use an ephemeris retrieved from NASA's Jet Propulsion Laboratory's Horizons[3] to compute the sky-plane speed of 2002 MS4.

---

[3] http://ssd.jpl.nasa.gov/

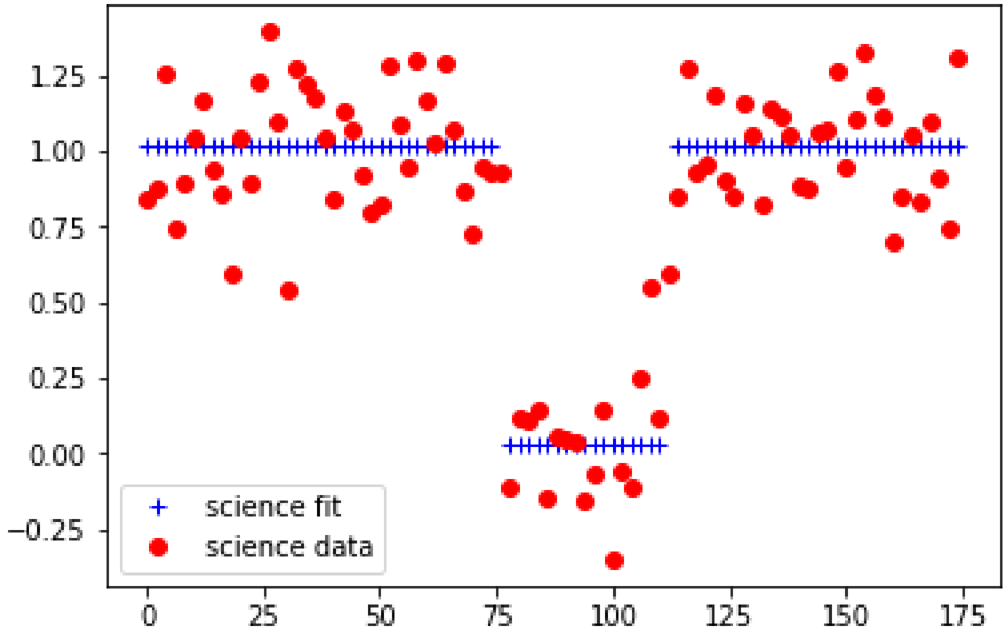

Figure 4.1: A light-curve for the occultation event on July 26, 2019. An obvious dip appears in the curve since the star is occulted by the MS_4.

I find that the inferred sizes for the two events are statistically different, implying, as epxected, that the two chords have different impact parameters. From the observed chords, we find the lower limit on the diameter of MS_4 is 823 ± 13 km (the larger of our two chord lengths). Each chord can be used to determine an estimate of the diameter of the body (see Equation 2.22). Using this approach we determine a best estimate for the diameter of 2002 MS_4 is approximately 1114 km. Thus, our estimated size of MS_4 is 1100 km $\geq$ d $\geq$ 820 km.

Table 4.3: Chord lengths for MS4 with its speeds adopted from JPL ephemeris

Obs date	T_d(s)	speed (km/s)	chord-length (km)
2020 July 26, 2019	35.054±0.544	23.47	822.72 ±12.77
2020 August 19, 2019	33.802±1.023	17.67	597.28 ±18.08

On 08-Aug-2020 as many as 116 telescopes participated in observations of a occultation of a star by 2002 MS4. This massive campaign was organized by the Lucky Star program. Using the combination of data from this event an equivalent diameter is about (800 ± 24) km was determined [64], consistent with our minimum diameter estimation (823 ± 13) km.

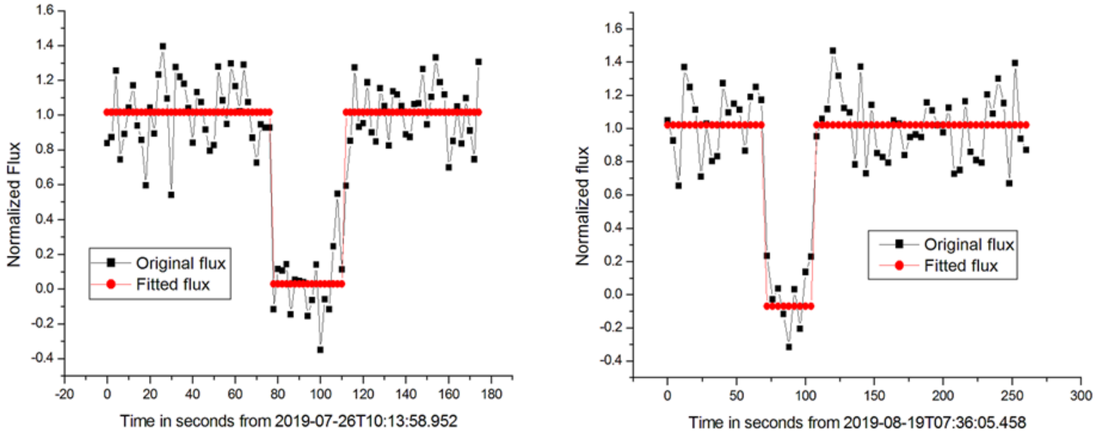

Figure 4.2: Occultation time series. Left panel: 26-Jul-2020 event. Right panel: 19-Aug-2020 event.

4.3 Geometric Albedo

Now that we have derived the absolute magnitude of MS_4 H_V and have a robust estimate of the object size one can determine the geometric albedo. Combining the geometric albedo with our previous determination of the phase we have already known its solar phase function (derived from Shevchenko's model). I estimate its geometric albedo as follows.

Using the phased curve from Chapter 3, I determine the absolute V magnitude. The size of an airless body and absolute magnitude are connected via the geometric albedo and V flux from the Sun via the formulae:

$$D = \frac{1336}{\sqrt{p_V}} 10^{-0.2H_V},$$

where D is the diameter of our target MS_4, and p_V is its geometric albedo [e.g. 68]. From my determination of the minimum diameter $D_m = 822 \pm 12$ km and measure of the absolute V magnitude $H_V = 3.56 \pm 0.03$ mag I determine the geometric V albedo to be

$$p_V \leq 0.099 \pm 0.004,$$

Chapter 5

A Portrait of 2002 MS4

Now that I have a measure of the major physical parameters of 2002 MS4 I consider the implications. First I consider the implications of the measured physical parameter for the thermal status of the object. Then I place the object's phase integral and albedo in the comparison to the asteroids to determine if 2002 MS4 has surface properties similar to asteroids.

5.1 Thermal Modeling

One can construct a thermal model of an airless body by considering the energy balance between absorbed and reflected plus emitted radiation. Under the assumption of a blackbody radiator the temperature can then be converted into a predict flux and compared to IR flux measurements. The Near Earth Asteroid Thermal Model (NEATM) [36] provides a simply parameterization of the expected temperature of an airless body.

Under the NEATM assumptions (very slow rotation, uniform composition and thermal equilibrium) the temperature on the surface of the body is given by

$$\epsilon \sigma T_{SS}^4 = \frac{(1-A)S}{\eta}$$

Where T_{SS} is the sub-solar temperature of the body, ϵ is the surface emissivity, σ the Stefan-Boltzman constant, A is the bond-Albedo, S is the solar constant at the surface of the object ($S = S_{\odot} \frac{1\mathrm{au}}{r_{au}}$ where $S_{\odot} = 1360.8 W/m^2$[48], and η is the so-called beaming factor. The beaming factor is larger than one for surface that emit most of their flux in the sun-ward direction and less than one for isotropic emission. The beaming factor also mimic the behaviour of a thermal inertia and is best thought of as a arbitrary normalization of the absorb flux (as opposed to the emitted flux normalization provided by ϵ). Clearly, within the thermal equation there is significant redundancy between A, η and, ϵ but each parameter is representative of a different physical effect.

The sub-solar temperature is used to model the surface temperature anywhere on the body as:

$$\begin{aligned} T &= T_{ss} \cos^{1/4}(\omega) \\ &= (\frac{(1-A)S}{\eta\epsilon\sigma})^{1/4} \cos^{1/4}(\omega) \end{aligned} \tag{5.1}$$

where ω is the angle between the sub-solar point and the point on the surface. Using this thermal profile for the object surface one can compute, under the assumption of a black-body radiator, the flux at any wavelength:

$$F(\lambda) = \int B(\lambda, T) d\mathbf{A} \cdot \mathbf{u}$$

Where here $d\mathbf{A} \cdot \mathbf{u}$ is a projected unit of area on the surface and B is the black-body equation.

Vilenius et al. [90] used observed 2002 MS4 from the Herschel Space Observatory and the Spritzer Space Telescope to compute a NEATM derived size estimate based on the observed thermal flux. They adopt a value of the emissivity of $\epsilon = 0.9$ based on laboratory measurements of ice [43] and use chi^2 minimization between the model and observed flux distribution to determine likely values of η, A and S_{proj} (the projected surface area). Their thermal-model constrained diameter of 2002 MS4 is $D = 934 \pm 47$ km with a Bond Albedo of $A = 0.025$ and $\eta = 1.06 \pm 0.06$. They convert the Bond Albedo to a geometric albedo of $p_V = 0.05 \pm 0.04$ and phase integral of $q = 0.5$ via the coupled equations of $A = p \times q$ and $q = 0.336p + 0.479$ [16].

One can determine an approximate value for the phase integral from the phase curve [89]:

$$q \approx 0.135 + 2.671\Phi(70^\circ),$$

where $\Phi(\alpha)$ is the value of the phase integral evaluated at 70^o. For the Shevchenko phase model (see Equation 2.19) we have:

$$\Phi(\alpha) = 10^{-0.4(\frac{\alpha}{1+\alpha}A+\alpha\times B)}$$

Thus we can find $q_V \approx 0.383 \pm 0.017$. The value of the Bond Albedo is $A = q \times p$ and thus, combining these measures we have

$$A_V = p_V \times q_V.$$

Therefore, A_V can be computed to be

$$A_V \leq 0.038 \pm 0.002.$$

The thermally fitting derived values of size and albedo are significantly different from those determined via occultation observation combined phase-curve measurements. In the thermal modelling the assumption of zero (very slow) rotation is made, this does not hold for 2002 MS4. The object is slowly rotating but likely not so slow that the night side will have fully cooled (i.e. there is significant residual heat from the thermal inertia). Thus, the leading 'dawn' side of the object will be warmer than predicted by the Equation 5.1 and the emitted flux per-unit area will be higher, resulting in the size of the object required to explain the emitted flux being smaller. The NEATM model attempts to compensate for the lack of a thermal inertia value by use of the η parameter, however, a more complete modelling that accounts for the rotation of 2002 MS4 is needed. This modeling is left to future work.

5.1.1 2002 MS4 versus the asteroids

Currently popular models of the formation of the outer solar system include a phase of dynamical instability during which the objects that formed in the Jupiter-Neptune region were scattered into different orbits. The family of such models are generally called Nice Model scenarios [50]. In some variants of this scenario objects that formed in the outer solar system end up in the asteroid belt and make up the C-type asteroids today [91]. If such models are correct then one might expect to find commonalities between the properties of the scattered (hot) Kuiper belt objects and the C-type asteroids. 2002 MS4 is currently a member of the hot component of the Kuiper belt. If the C-type asteroids did originate in the same zone as 2002 MS4 then one might expect them to share a phase/albedo relation.

In Figure 5.1, I show the both occultation/light-curve derived and thermal model derived geometric albedo of 2002 MS_4 as compared to the values for 33 well-measured asterods [5]. Although the thermal model derived albedo is somewhat discordant with the asteroid relation my occultation determined value is more consistent with this relationship. There is consistency between the phase/albedo of 2002 MS2 and that of the asteroids, perhaps the share some common surface properties.

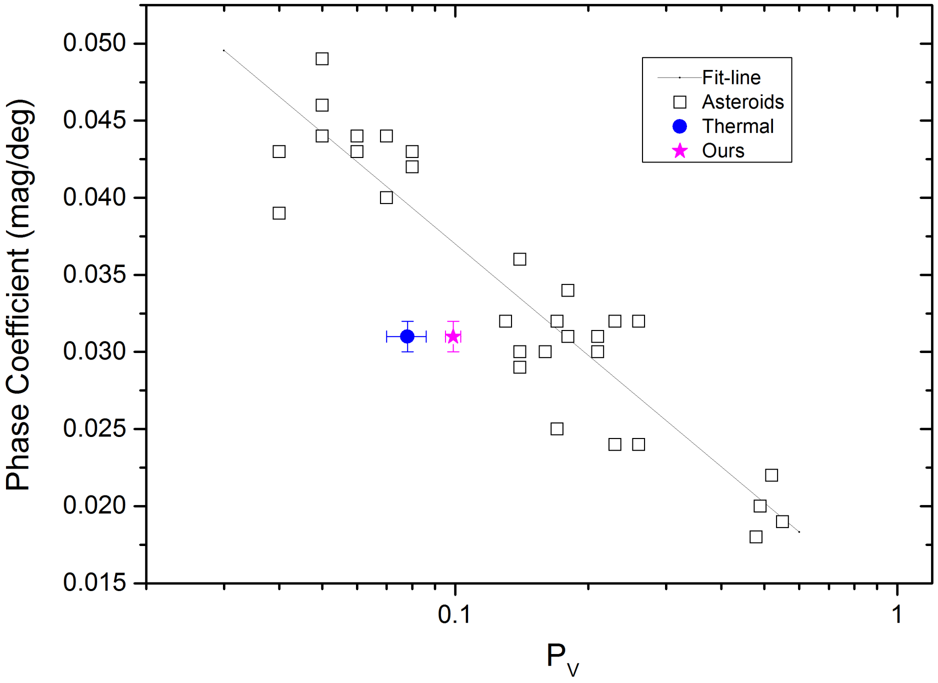

Figure 5.1: Phase coefficient vs. geometric albedo. Values for MS4 determined using occultation (red) and thermal (blue) based size measurements. Also shown are the vlues for 33 well-measured asteroids along with a linear fit to those data[5].

Belskaya et al.[5] find that the amplitude of opposition effect (OE) is correlated with an asteroid's abledo and type. The OE is largest for modest albedo asteroids, but decreasing for dark and high albedo asteroids. The OE is quantified as the ratio of the intensity at 0.3^o to that at 5^o. Using the derived Shevchenko's phase model

(Equation 2.19) we can obtain the value of the OE,

$$\frac{I_{0.3}}{I_5} = 10^{0.4\times((1/1.3-1/6)A+4.7B)} \approx 10^{0.241A+1.88B}$$

For MS4, therefore, based on my best-fit values for the parameters A and B and their uncertainties, I find:

$$\frac{I_{0.3}}{I_5} \approx 1.44 \pm 0.02.$$

Using the data from [5] I compare the OE - geometric albedo relation for 2002 MS4 with that of a variety of asteroids (see Figure!5.2). If the C-type asteroids and 2002 MS4 share a common origin we might expect them to share a grouping in the OE-albedo space. Figure 5.2 shows that that 2002 MS4 is located between the C-type asteroids (population posited to share an origin with hot KBOs) and the M-type asteroids (that is the metallic asteroids) that do not share a formation origin with the hot KBOs. 2002 MS4's OE/albedo correlation is more consistent with M-type than C-type asteroids. Therefore, we can draw the conclusion that MS4 is not C-type like. I find, based on phase/albedo correlations, that 2002 MS4 and the C-type asteroids have differing surface compositions, suggesting that they do not share a common formation location. Here we include a reminder table **??** of

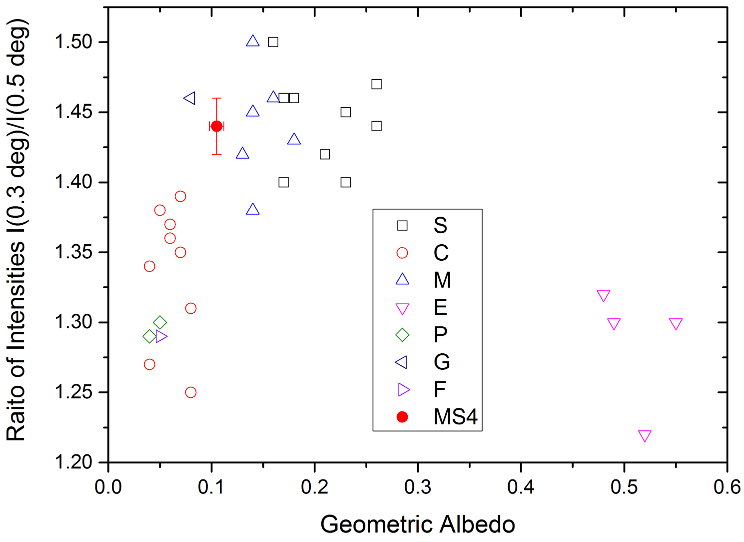

Figure 5.2: The type of MS4 from its ratio of intensities of I(0.3 deg)/I(5 deg)

different type of asteroids.

Table 5.1: Asteroid Types

Asteroid Type	Composition
S	Silicaceous
C	Carbon-rich
M	Mostly composed of metal
E	Contains enstatite (MgSiO3)
P	Unique compositions, possibly organic-rich
G	Subcategory of C-type asteroids
F	Uncommon type of C-type asteroid

5.2 Summary

This dissertation is aimed to utilize CFHT/MegaCam archival images to perform precise photometry of the faint and distant but large KBO, (307261) 2002 MS_4 (MS4).

Using observations stars occulted by 2002 MS4 I have determined the minimum physical size of this object. My estimate based on two single chord observations are fully consistent with the more constrained result found during an observing campaign that enlisted 130 individual telescopes and observers. The estimated size derived from occultations is formally inconsistent with that obtained via thermal model fits, likely indicating that the thermal models are too simplistic and perhaps more complex models that include rotation effects and thermal inertia are needed.

Using time-series data obtained from the CFHT MegaCam archive I have constructed a high precision light-curve for 2002 MS4. Using the light-curve data I determined a rotation period and amplituded for 2002 MS4. The light-curve amplitude is low, consistent with the nearly spherical shape found during the occultation campaign while the rotation period is consistent with that found for similar solar system bodies.

By combining ground-based photometry with the space-based photometry obtained from New Horizons/LORRI I have constructed a complete phase curve for 2002 MS4. I find that the two-parameter HG phase function does not provide a good representation of the data while the three-parameter Shevchenko model provides a reasonable representation of the data. This three parameter model provides the opportunity to do comparative studies with asteroid families without introducing the full complexity of Hapke's phase model. The large number of parameters would have provide an over-fit to the spare data set available.

Table 5.2 summarizes the results of my measurements and the derived physical parameters for 2002 MS4.

Combining the size estimate from occultations with the measured phase curve enables a comparison between the Opposition Effect, albedo and phase ratio of 2002 MS4 with that of various asteroid families. Based on this comparison I find no evidence, within this portrait of MS4 surface characteristics, to support the concept that the majority of the C-type asteroids formed with the hot-component KBOs.

Table 5.2: Parameters of MS4 by our solution and some references

item	our solution	other solution	reference
H_V (mag)	3.56 ± 0.03	3.63	[82]
Phase coefficient	0.17 ± 0.01		
Rotation period	14.25 hr	7.33 hr	[86]
Rotation amplitude	0.12 ± 0.01 mag	0.05 mag	[86]
Diameter	$> 822 \pm 13$ km	800 ± 24 km	[64]
Phase integral	0.38 ± 0.02		
Geometric albedo	$\leq 0.099 \pm 0.004$	0.051	[90]
Bond albedo	$\leq 0.038 \pm 0.002$		

5.3 Future work.

The rotation period of 2002 MS4 determined in this analysis should be confirmed. Such confirmation would require an observing campaign that obtained nearly continuous data for multiple nights such that aliasing between the possible 14 and 7-hour periods could be removed.

As suggested above, when a more robustly determined rotation period is available, a more complete thermal model for the surface of 2002 MS4 that considers rotation and thermal inertia should be constructed such that a thermal diameter consistent with occultation measures could be determined. Such a model should also take into account the likely surface material of 2002 MS4, which is expected to be well determined by very recently obtained JWST IR spectra.

The physical parameters reported of 2002 MS4 reported in this thesis will be valuable inputs into future modeling work.

Bibliography

[1] C Alard and Robert H Lupton. A method for optimal image subtraction. *The Astrophysical Journal*, 503(1):325, 1998.

[2] Christophe Alard. Image subtraction using a space-varying kernel. *Astronomy and Astrophysics Supplement Series*, 144(2):363–370, 2000.

[3] MA Barucci, M Fulchignoni, M Birlan, A Doressoundiram, J Romon, and H Boehnhardt. Analysis of trans-neptunian and centaur colours: continuous trend or grouping? *Astronomy & Astrophysics*, 371(3):1150–1154, 2001.

[4] Maria Antonietta Barucci, IN Belskaya, Marcello Fulchignoni, and Mirel Birlan. Taxonomy of centaurs and trans-neptunian objects. *The Astronomical Journal*, 130(3):1291, 2005.

[5] IN Belskaya and VG Shevchenko. Opposition effect of asteroids. *Icarus*, 147(1):94–105, 2000.

[6] Irina N Belskaya, Anny-Chantal Levasseur-Regourd, Yuriy G Shkuratov, and Karri Muinonen. Surface properties of kuiper belt objects and centaurs from photometry and polarimetry. *The Solar System Beyond Neptune*, pages 115–127, 2008.

[7] J. Bergeron. Proceedings of the Twenty-first General Assembly. *Transactions of the International Astronomical Union, Series B*, 21B, January 1992.

[8] E. Bertin and S. Arnouts. Sextractor: Software for source extraction. *A & A Sup.*, 117:393–404, Jun 1996.

[9] M. S. Bessell, F. Castelli, and B. Plez. Model atmospheres broad-band colors, bolometric corrections and temperature calibrations for O - M stars. A&A, 333:231–250, May 1998.

[10] Michael S. Bessell. Standard Photometric Systems. ARA&A, 43(1):293–336, September 2005.

[11] François Bonnarel, Pierre Fernique, Olivier Bienaymé, Daniel Egret, Françoise Genova, Mireille Louys, François Ochsenbein, Marc Wenger, and James G Bartlett. The aladin interactive sky atlas. *ASTROPHYSICS*, 2000.

[12] Olivier Boulade, Xavier Charlot, P Abbon, Stephan Aune, Pierre Borgeaud, Pierre-Henri Carton, M Carty, J Da Costa, H Deschamps, D Desforge, et al. Megacam: the new canada-france-hawaii telescope wide-field imaging camera. In *Instrument Design and Performance for Optical/Infrared Ground-based Telescopes*, volume 4841, pages 72–81. International Society for Optics and Photonics, 2003.

[13] Edward Bowell, Bruce Hapke, Deborah Domingue, Kari Lumme, Jouni Peltoniemi, and Alan W Harris. Application of photometric models to asteroids. *Asteroids II*, pages 524–556, 1989.

[14] F Braga-Ribas, B Sicardy, JL Ortiz, C Snodgrass, F Roques, R Vieira-Martins, JIB Camargo, M Assafin, R Duffard, E Jehin, et al. A ring system detected around the centaur (10199) chariklo. *Nature*, 508(7494):72–75, 2014.

[15] AGA Brown, Antonella Vallenari, T Prusti, JHJ De Bruijne, C Babusiaux, CAL Bailer-Jones, M Biermann, Dafydd Wyn Evans, Laurent Eyer, Femke Jansen, et al. Gaia data release 2-summary of the contents and survey properties. *Astronomy & astrophysics*, 616:A1, 2018.

[16] M. J. Brucker, W. M. Grundy, J. A. Stansberry, J. R. Spencer, S. S. Sheppard, E. I. Chiang, and M. W. Buie. High albedos of low inclination Classical Kuiper belt objects. Icarus, 201(1):284–294, May 2009.

[17] Marc W Buie, Rodrigo Leiva, John M Keller, Josselin Desmars, Bruno Sicardy, JJ Kavelaars, Terry Bridges, Robert Weryk, Dave Herald, Sean L Haley, et al. A single-chord stellar occultation by the extreme trans-neptunian object (541132) leleākūhonua. *The Astronomical Journal*, 159(5):230, 2020.

[18] AF Cheng, HA Weaver, SJ Conard, MF Morgan, O Barnouin-Jha, JD Boldt, KA Cooper, EH Darlington, MP Grey, JR Hayes, et al. Long-range reconnaissance imager on new horizons. *Space Science Reviews*, 140(1):189–215, 2008.

[19] Andrew F Cheng, HA Weaver, SJ Conard, MF Morgan, O Barnouin-Jha, JD Boldt, KA Cooper, EH Darlington, MP Grey, JR Hayes, et al. Long-range reconnaissance imager on new horizons. *New Horizons*, pages 189–215, 2009.

[20] J de Kat, S Aune, O Boulade, P Borgeaud, P-H Carton, M Carty, X Charlot, D Desforge, D Eppellé, P Gallais, et al. Megacam: The next generation wide-field camera for cfht. In *Optical Detectors For Astronomy II*, pages 111–117. Springer, 2000.

[21] R Duffard, JL Ortiz, A Thirouin, P Santos-Sanz, and N Morales. Transneptunian objects and centaurs from light curves. *Astronomy & Astrophysics*, 505(3):1283–1295, 2009.

[22] James L Elliot, Michael James Person, CA Zuluaga, Amanda Sachie Bosh, Elisabeth R Adams, Timothy C Brothers, Amanda AS Gulbis, Stephen E Levine, Matthew Lockhart, Amanda M Zangari, et al. Size and albedo of kuiper belt object 55636 from a stellar occultation. *Nature*, 465(7300):897–900, 2010.

[23] HA Flewelling, EA Magnier, KC Chambers, JN Heasley, C Holmberg, ME Huber, W Sweeney, CZ Waters, A Calamida, S Casertano, et al. The pan-starrs1 database and data products. *The Astrophysical Journal Supplement Series*, 251(1):7, 2020.

[24] W. M. Folkner, P. Charlot, M. H. Finger, J. G. Williams, O. J. Sovers, Xx Newhall, and Jr. Standish, E. M. Determination of the extragalactic-planetary frame tie from joint analysis of radio interferometric and lunar laser ranging measurements. A&A, 287:279–289, July 1994.

[25] Wesley C. Fraser and Michael E. Brown. The Hubble Wide Field Camera 3 Test of Surfaces in the Outer Solar System: The Compositional Classes of the Kuiper Belt. ApJ, 749(1):33, April 2012.

[26] Wesley C. Fraser, Rosemary E. Pike, Michaël Marsset, Megan E. Schwamb, Michele T. Bannister, Laura Buchanan, J. J. Kavelaars, Susan D. Benecchi, Nicole J. Tan, Nuno Peixinho, Stephen D. J. Gwyn, Mike Alexandersen, Ying-Tung Chen, Brett Gladman, and Kathryn Volk. Col-OSSOS: The Two Types of Kuiper Belt Surfaces. PSJ, 4(5):80, May 2023.

[27] M. Fukugita, T. Ichikawa, J. E. Gunn, M. Doi, K. Shimasaku, and D. P. Schneider. The Sloan Digital Sky Survey Photometric System. AJ, 111:1748, April 1996.

[28] L. Girardi, G. Bertelli, A. Bressan, C. Chiosi, M. A. T. Groenewegen, P. Marigo, B. Salasnich, and A. Weiss. Theoretical isochrones in several photometric systems. I. Johnson-Cousins-Glass, HST/WFPC2, HST/NICMOS, Washington, and ESO Imaging Survey filter sets. A&A, 391:195–212, August 2002.

[29] L. Girardi, E. K. Grebel, M. Odenkirchen, and C. Chiosi. Theoretical isochrones in several photometric systems. II. The Sloan Digital Sky Survey ugriz system. A&A, 422:205–215, July 2004.

[30] Brett Gladman, Brian G Marsden, and Christa VanLaerhoven. Nomenclature in the outer solar system. *The Solar System Beyond Neptune*, 43, 2008.

[31] E. W. Greisen and R. H. Harten. An Extension of FITS for Groups of Small Arrays of Data. A&AS, 44:371, June 1981.

[32] Stephen D. J. Gwyn. MegaPipe: The MegaCam Image Stacking Pipeline at the Canadian Astronomical Data Centre. PASP, 120(864):212, February 2008.

[33] Stephen D. J. Gwyn, Norman Hill, and JJ Kavelaars. Solar System Object Image Search: A precovery search engine. In S. R. Chesley, A. Morbidelli, R. Jedicke, and D. Farnocchia, editors, *Asteroids: New Observations, New Models*, volume 318 of *IAU Symposium*, pages 270–273, Jan 2016.

[34] Bruce Hapke. *Theory of Reflectance and Emittance Spectroscopy.* Cambridge University Press, 2 edition, 2012.

[35] A. W. Harris, J. W. Young, E. Bowell, L. J. Martin, R. L. Millis, M. Poutanen, F. Scaltriti, V. Zappala, H. J. Schober, H. Debehogne, and K. W. Zeigler. Photoelectric observations of asteroids 3, 24, 60, 261, and 863. Icarus, 77(1):171–186, January 1989.

[36] Alan W. Harris. A Thermal Model for Near-Earth Asteroids. Icarus, 131(2):291–301, February 1998.

[37] William E. Harris. A Comment on Image Detection and the Definition of Limiting Magnitude. PASP, 102:949, August 1990.

[38] D. S. Hayes and D. W. Latham. A rediscussion of the atmospheric extinction and the absolute spectral-energy distribution of Vega. ApJ, 197:593–601, May 1975.

[39] C. Hazard, J. Sutton, A. N. Argue, Cecilia M. Kenworthy, L. V. Morrison, and C. A. Murray. Accurate Radio and Optical Positions of 3C273B. *Nature Physical Science*, 233(40):89–91, October 1971.

[40] AN Heinze and Daniel DeLahunta. The rotation period and light-curve amplitude of kuiper belt dwarf planet 136472 makemake (2005 fy9). *The Astronomical Journal*, 138(2):428, 2009.

[41] John M. Hill, Richard F. Green, and James H. Slagle. The Large Binocular Telescope. In Larry M. Stepp, editor, *Society of Photo-Optical Instrumentation Engineers (SPIE) Conference Series*, volume 6267 of *Society of Photo-Optical Instrumentation Engineers (SPIE) Conference Series*, page 62670Y, June 2006.

[42] Jason D Hofgartner, Bonnie J Buratti, Susan D Benecchi, Ross A Beyer, Andrew Cheng, James T Keane, Tod R Lauer, Catherine B Olkin, Joel W Parker, Kelsi N Singer, et al. Photometry of kuiper belt object (486958) arrokoth from new horizons lorri. *Icarus*, 356:113723, 2021.

[43] Jr. Hovis, W. A. and William R. Callahan. Infrared Reflectance Spectra of Igneous Rocks, Tuffs, and Red Sandstone from 0.5 to 22 mu. *Journal of the Optical Society of America (1917-1983)*, 56(5):639, May 1966.

[44] David Jewitt and Jane Luu. Discovery of the candidate kuiper belt object 1992 qb1. *Nature*, 362(6422):730–732, 1993.

[45] K. Jordi, E. K. Grebel, and K. Ammon. Empirical color transformations between SDSS photometry and other photometric systems. A&A, 460(1):339–347, December 2006.

[46] Henry C. King. *The History of the Telescope.* Charles Griffin and Company Limited, London, 1955.

[47] Ivan R King. The profile of a star image. *Publications of the Astronomical Society of the Pacific*, 83(492):199, 1971.

[48] Greg Kopp and Judith L. Lean. A new, lower value of total solar irradiance: Evidence and climate significance. Geophys. Res. Lett., 38(1):L01706, January 2011.

[49] Arlo U. Landolt. UBVRI Photometric Standard Stars in the Magnitude Range 11.5 < V < 16.0 Around the Celestial Equator. AJ, 104:340, July 1992.

[50] Harold F. Levison, Alessandro Morbidelli, Christa Van Laerhoven, Rodney Gomes, and Kleomenis Tsiganis. Origin of the structure of the Kuiper belt during a dynamical instability in the orbits of Uranus and Neptune. Icarus, 196(1):258–273, July 2008.

[51] Light, Michael and Chaikin, Andrew. *Full Moon.* Knopf, 1999.

[52] N. R. Lomb. Precise observations of minor planets at Sydney Observatory during 1981. *Journal and Proceedings of the Royal Society of New South Wales*, 115:5–8, January 1982.

[53] Nicholas R Lomb. Least-squares frequency analysis of unequally spaced data. *Astrophysics and space science*, 39(2):447–462, 1976.

[54] J. B. Oke. Absolute Spectral Energy Distributions for White Dwarfs. ApJS, 27:21, February 1974.

[55] J. B. Oke and J. E. Gunn. Secondary standard stars for absolute spectrophotometry. ApJ, 266:713–717, March 1983.

[56] José L Ortiz, Bruno Sicardy, Julio IB Camargo, Pablo Santos-Sanz, and Felipe Braga-Ribas. Stellar occultations by trans-neptunian objects: From predictions to observations and prospects for the future. In *The Trans-Neptunian Solar System*, pages 413–437. Elsevier, 2020.

[57] José Luis Ortiz, Pablo Santos-Sanz, B Sicardy, G Benedetti-Rossi, D Bérard, N Morales, R Duffard, F Braga-Ribas, U Hopp, C Ries, et al. The size, shape, density and ring of the dwarf planet haumea from a stellar occultation. *Nature*, 550(7675):219–223, 2017.

[58] E. Paunzen and T. Vanmunster. Peranso – light curve and period analysis software. *Astronomische Nachrichten*, 337(3):239–245, 2016.

[59] Nuno Peixinho, Audrey Thirouin, Stephen C Tegler, Romina P Di Sisto, Audrey Delsanti, Aurélie Guilbert-Lepoutre, and James G Bauer. From centaurs to comets: 40 years. In *The Trans-Neptunian Solar System*, pages 307–329. Elsevier, 2020.

[60] Simon B Porter, John R Spencer, Susan Benecchi, Anne J Verbiscer, Amanda M Zangari, Harold A Weaver, Tod R Lauer, Alex H Parker, Marc W Buie, Andrew F Cheng, et al. The first high-phase observations of a kbo: New horizons imaging of (15810) 1994 jr1 from the kuiper belt. *The Astrophysical Journal Letters*, 828(2):L15, 2016.

[61] WH Press, SA Teukolsky, WT Vetterling, and BP Flannery. *Numerical recipes in C (2nd ed.)*. New York: Cambridge Univ.Press, 1992.

[62] David L Rabinowitz, Bradley E Schaefer, and Suzanne W Tourtellotte. The diverse solar phase curves of distant icy bodies. i. photometric observations of 18 trans-neptunian objects, 7 centaurs, and nereid. *The Astronomical Journal*, 133(1):26, 2006.

[63] René Racine. Astronomical seeing at mauna kea and in particular at the cfht. In *International Astronomical Union Colloquium*, volume 79, pages 235–243. Cambridge University Press, 1984.

[64] Flavia L Rommel, Felipe Braga-Ribas, Mónica Vara-Lubiano, Jose L Ortiz, Josselin Desmars, Bruno E Morgado, Gustavo Benedetti-Rossi, Bruno Sicardy, Roberto Vieira-Martins, Julio IB Camargo, et al. Evidence of topographic features on (307261) 2002 ms4 surface. Technical report, Copernicus Meetings, 2021.

[65] F. Roques, M. Moncuquet, and B. Sicardy. Stellar occultations by small bodies - Diffraction effects. AJ, 93:1549–1558, June 1987.

[66] Jeffrey D Scargle. Studies in astronomical time series analysis. ii-statistical aspects of spectral analysis of unevenly spaced data. *The Astrophysical Journal*, 263:835–853, 1982.

[67] Hilke E Schlichting, Cesar I Fuentes, and David E Trilling. Initial planetesimal sizes and the size distribution of small kuiper belt objects. *The Astronomical Journal*, 146(2):36, 2013.

[68] Michael K. Shepard. *Introduction to Planetary Photometry.* Cambridge University Press, 2017.

[69] Scott S Sheppard and David C Jewitt. Time-resolved photometry of kuiper belt objects: Rotations, shapes, and phase functions. *The Astronomical Journal*, 124(3):1757, 2002.

[70] VG Shevchenko. Analysis of asteroid brightness-phase relations. *Solar System Research*, 31(3):219, 1997.

[71] D. L. Shupe, Mehdrdad Moshir, J. Li, D. Makovoz, R. Narron, and R. N. Hook. The SIP Convention for Representing Distortion in FITS Image Headers. In P. Shopbell, M. Britton, and R. Ebert, editors, *Astronomical Data Analysis Software and Systems XIV*, volume 347 of *Astronomical Society of the Pacific Conference Series*, page 491, December 2005.

[72] Bruno Sicardy, JL Ortiz, M Assafin, Emmanuel Jehin, A Maury, Emmanuel Lellouch, R Gil Hutton, F Braga-Ribas, Francois Colas, Daniel Hestroffer, et al. A pluto-like radius and a high albedo for the dwarf planet eris from an occultation. *Nature*, 478(7370):493–496, 2011.

[73] Robert F Stellingwerf. Period determination using phase dispersion minimization. *The Astrophysical Journal*, 224:953–960, 1978.

[74] S Alan Stern, F Bagenal, K Ennico, GR Gladstone, WM Grundy, WB McKinnon, JM Moore, CB Olkin, JR Spencer, HA Weaver, et al. The pluto system: Initial results from its exploration by new horizons. *Science*, 350(6258), 2015.

[75] S Alan Stern, John R Spencer, Anne Verbiscer, Heather E Elliott, and Simon P Porter. Plans for and initial results from the exploration of the kuiper belt by new horizons. In *The Trans-Neptunian Solar System*, pages 379–394. Elsevier, 2020.

[76] SA Stern, HA Weaver, JR Spencer, and HA Elliott. The new horizons kuiper belt extended mission. *Space Science Reviews*, 214(4):1–23, 2018.

[77] SA Stern, HA Weaver, JR Spencer, CB Olkin, GR Gladstone, WM Grundy, JM Moore, DP Cruikshank, HA Elliott, WB McKinnon, et al. Initial results from the new horizons exploration of 2014 mu69, a small kuiper belt object. *Science*, 364(6441), 2019.

[78] Peter B Stetson. On the growth-curve method for calibrating stellar photometry with ccds. *Publications of the Astronomical Society of the Pacific*, 102(654):932, 1990.

[79] S. C. Tegler, W. Romanishin, G. J. Consolmagno, and S. J. Two Color Populations of Kuiper Belt and Centaur Objects and the Smaller Orbital Inclinations of Red Centaur Objects. AJ, 152(6):210, December 2016.

[80] Stephen C Tegler and W Romanishin. Two distinct populations of kuiper-belt objects. *Nature*, 392(6671):49–51, 1998.

[81] Stephen C Tegler, W Romanishin, and SJ GJ Consolmagno. Color patterns in the kuiper belt: A possible primordial origin. *The Astrophysical Journal Letters*, 599(1):L49, 2003.

[82] Stephen C Tegler, W Romanishin, and SJ GJ Consolmagno. Two color populations of kuiper belt and centaur objects and the smaller orbital inclinations of red centaur objects. *The Astronomical Journal*, 152(6):210, 2016.

[83] Ph Thébault and A Doressoundiram. Colors and collision rates within the kuiper belt: problems with the collisional resurfacing scenario. *Icarus*, 162(1):27–37, 2003.

[84] Philippe Thébault. A numerical check of the collisional resurfacing scenario. In *The First Decadal Review of the Edgeworth-Kuiper Belt*, pages 233–241. Springer, 2004.

[85] A Thirouin, JL Ortiz, R Duffard, P Santos-Sanz, FJ Aceituno, and N Morales. Short-term variability of a sample of 29 trans-neptunian objects and centaurs. *Astronomy & Astrophysics*, 522:A93, 2010.

[86] Audrey Thirouin. *Study of trans-neptunian objects using photometric techniques and numerical simulations.* PhD thesis, University of Granada, Spain, January 2013.

[87] C. A. Trujillo, M. E. Brown, E. F. Helin, S. Pravdo, K. Lawrence, M. Hicks, C. Nash, A. B. Jordan, S. Staples, M. Schwartz, and B. G. Marsden. 2002 MS4,. *Minor Planet Electronic Circulars*, 2002-W27, November 2002.

[88] Anne J. Verbiscer, Paul Helfenstein, Simon B. Porter, Susan D. Benecchi, J. J. Kavelaars, Tod R. Lauer, Jinghan Peng, Silvia Protopapa, John R. Spencer, S. Alan Stern, Harold A. Weaver, Marc W. Buie, Bonnie J. Buratti, Catherine B. Olkin, Joel Parker, Kelsi N. Singer, Leslie A. Young, and New Horizons Science Team. The Diverse Shapes of Dwarf Planet and Large KBO Phase Curves Observed from New Horizons. PSJ, 3(4):95, April 2022.

[89] Anne J. Verbiscer and Joseph Veverka. Estimating phase integrals: A generalization of Russell's law. Icarus, 73(2):324–329, February 1988.

[90] Esa Vilenius, C. Kiss, M. Mommert, T. Muller, P. Santos-Sanz, A. Pal, J. Stansberry, M. Mueller, N. Peixinho, S. Fornasier, E. Lellouch, A. Delsanti, A. Thirouin, R. Duffard, and J. Ortiz. TNOs are Cool: Analysis of Classical Kuiper Belt Objects from Herschel Space Observatory Data. In *AAS/Division for Planetary Sciences Meeting Abstracts #44*, volume 44 of *AAS/Division for Planetary Sciences Meeting Abstracts*, page 402.03, October 2012.

[91] Kevin J. Walsh, A. Morbidelli, S. N. Raymond, D. P. O'Brien, and A. M. Mandell. Populating the asteroid belt from two parent source regions due to the migration of giant planets—"The Grand Tack". *Meteoritics & Planetary Science*, 47(12):1941–1947, December 2012.

[92] Brian D. D. Warner. *A Practical Guide to Lightcurve Photometry and Analysis.* Springer, 2016.

[93] HA Weaver, AF Cheng, F Morgan, HW Taylor, SJ Conard, JI Nunez, DJ Rodgers, TR Lauer, WM Owen, JR Spencer, et al. In-flight performance and calibration of the long range reconnaissance imager (lorri) for the new horizons mission. *Publications of the Astronomical Society of the Pacific*, 132(1009):035003, 2020.

[94] G. W. Wetherill and G. R. Stewart. Accumulation of a swarm of small planetesimals. Icarus, 77(2):330–357, February 1989.

[95] Alexandra Witze. Cosmic collision created'snowman'mu. sub. 69–the farthest world ever explored. *Nature*, 565(7738):142–144, 2019.